

Dynamical decoherence of a qubit coupled to a quantum dot or the SYK black hole

Klaus M. Frahm¹ and Dima L. Shepelyansky¹

Laboratoire de Physique Théorique, IRSAMC, Université de Toulouse, CNRS, UPS, 31062 Toulouse, France

Dated: 28 April 2018

Abstract. We study the dynamical decoherence of a qubit weakly coupled to a two-body random interaction model (TBRIM) describing a quantum dot of interacting fermions or the Sachdev-Ye-Kitaev (SYK) black hole model. We determine the rates of qubit relaxation and dephasing for regimes of dynamical thermalization of the quantum dot or of quantum chaos in the SYK model. These rates are found to correspond to the Fermi golden rule and quantum Zeno regimes depending on the qubit-fermion coupling strength. An unusual regime is found where these rates are practically independent of TBRIM parameters. We push forward an analogy between TBRIM and quantum small-world networks with an explosive spreading over exponentially large number of states in a finite time being similar to six degrees of separation in small-world social networks. We find that the SYK model has approximately two-three degrees of separation.

PACS. XX.XX.XX No PACS code given

1 Introduction

The problem of qubit decoherence is crucial for the process of quantum measurement [1] and the field of quantum information and computation [2]. The experimental realization of superconducting qubits [3, 4] extended this problem to a world of large objects due to a macroscopic size of superconducting qubits (see e.g. [5, 6, 7]). In theoretical considerations the decoherence of a qubit is usually due to the contact with a thermal bath, weak measurements or other statistical systems characterizing a detector (or sensor) being in a contact with the qubit [5, 6, 7]. A model of a deterministic detector, whose evolution takes place in a regime of quantum chaos, was studied in [8] demonstrating the emergence of dynamical decoherence of a qubit in absence of any thermal bath, noise and external randomness. We extend this research line [8] considering as a deterministic detector a quantum dot with interacting fermions or the Sachdev-Ye-Kitaev (SYK) black hole model.

The question about dynamical decoherence is closely related to the problem of quantum dynamical thermalization and random matrix theory (RMT) invented by Wigner [9, 10, 11] for the description of complex atoms and nuclei. While the properties of one-particle quantum chaos and their link with RMT are now mainly understood (see e.g. [12, 13, 14]), the analysis of many-body quantum systems is more difficult due to the complexity of quantum many-body systems (QMBS). Furthermore RMT is only an approximation to QMBS since in nature we have only two-body interactions and hence the exponentially large Hamiltonian matrix of QMBS has only a small fraction of non-zero matrix elements. To capture this feature a

two-body random interaction model of fermions (TBRIM) was proposed in [15, 16, 17, 18] and it was shown that at strong interactions this model is characterized by RMT level spacing statistics. The first numerical results and analytical arguments for a critical interactions strength in TBRIM with a finite level spacing Δ between one-particle orbitals was proposed by Sven Åberg in [19, 20]. For the TBRIM the Åberg criterion for onset of quantum chaos and dynamical thermalization has the form

$$\delta E = E - E_g > \delta E_{\text{ch}} \approx g^{2/3} \Delta, \quad g = \Delta/U, \quad (1)$$

where U is a typical strength of two-body interactions, Δ is an average one-particle level spacing in a finite size quantum dot with interacting fermions, E_g is the ground state energy of the quantum dot when all electrons are below the Fermi energy E_F and E is the energy of an excited eigenstate. The dimensional parameter $g \gg 1$ is assumed to be large playing the role of the conductance of a quantum dot with weakly interacting electrons. The validity of the Åberg criterion (1) for the emergence of RMT level statistics was confirmed in first numerical simulations [19, 20] and in independent more extensive analytical and numerical studies for 3 particles in a quantum dot [21], TBRIM [22], spin glass shards [23], quantum computers with imperfections [24, 25, 26]. Advanced theoretical arguments developed in [27, 28] confirm the relation (1) for interacting fermions in a quantum dot.

While the validity of the Åberg criterion for emergence of RMT in TBRIM and other models is satisfactory confirmed by numerical and analytical studies, a dynamical thermalization conjecture (DTC), which is used for

the derivation of (1), is more difficult for the numerical verification since it requires the knowledge not only of the eigenvalues but also the computation of eigenstates that is more difficult. The TBRIM numerical results [29] for the probability distribution over one-particle orbitals, averaged over many random realizations, showed a certain proximity to the Fermi-Dirac distribution expected from the quantum statistical mechanics [30]. The validity of the Fermi-Dirac distribution for a single eigenstate was demonstrated numerically for eigenstates of a quantum computer with imperfections and residual inter-qubit couplings [26]. We stress that the DTC is proposed for a purely isolated system without any contact to an external thermostat and the dynamical thermalization is only due to internal many-body quantum chaos.

However, for a single eigenstate the fluctuations of probabilities n_k on one-particle orbitals are significant requiring heavy large matrix diagonalizations to obtain a reasonable agreement with the Fermi-Dirac distribution [26]. Another method was developed for nonlinear disordered chains described by classical Hamiltonian equations [31, 32]. It is based on the computation of entropy S and energy E tracing the dependence $S(E)$ which is obtained as an implicit function from $S(T)$ and $E(T)$ where T is the system temperature appearing due to dynamical thermalization in a completely isolated system without any contact to an external thermostat. Since the quantities S and E are extensive [30] their fluctuations are reduced due to self-averaging. The dependence $S(E)$ for many-body quantum systems was computed for bosons in disordered Bose-Hubbard model in 1D [33] and for spinless fermions in the TBRIM [34]. These studies demonstrated the stability and efficiency of $S(E)$ -computations confirming validity of the DTC for many-body interacting quantum systems. The dynamical thermalization of an individual eigenstate was also demonstrated in [33, 34]. At present the interest of many-body interacting quantum systems is also growing in the context of many-body localization (MBL) and the eigenstate thermalization hypothesis (ETH) (see e.g. [35, 36, 37, 38]).

Another bust of interest to the TBRIM type models appeared due to the recent results of Sachdev-Ye-Kitaev for a strange metal and its links to a quantum black hole model in 1+1 dimensions (coordinate plus time) known now as the SYK black hole [39, 40, 41]. In fact, the SYK model, in its fermionic formulation, corresponds to the TBRIM considered in the limit of very strong interactions with a conductance close to zero $g \rightarrow 0$. The analogy between physical representations of the SYK model attracted a significant interest of researchers in quantum gravity, many-body systems, RMT and quantum chaos (see e.g. [42, 43, 44]). Recent advanced numerical and analytical results on the validity of RMT for the SYK model with Majorana fermions are reported in [45, 46, 47].

In this work we study the dynamical decoherence of a qubit coupled to the TBRIM model. This is a completely isolated system in absence of noise, thermal bath and external decoherence. At $g \gg 1$ the qubit is coupled to a quantum dot of weakly interacting fermions with our

main interest being focused on the regime of dynamical thermalization when the Åberg criterion (1) is satisfied. At $g \ll 1$ our model becomes equivalent to the SYK black hole model with a qubit coupled to it. We note that the decoherence of a qubit coupled to a quantum black hole is extensively discussed in the context of the black hole problem of information loss for the infalling observer (see [48] and Refs. therein). We expect that the dynamical qubit decoherence considered here will be useful for a better understanding of this problem.

The paper is composed as follows: In Section 2 the TBRIM is introduced and some of its properties are reminded while in Section 3 the additional qubit-fermion coupling is introduced. The qubit relaxation rates are studied in Section 4 and in Section 5 the link to a quantum small-world networks is discussed. In Section 6 results of the residual level of qubit density matrix relaxation at long times are described and Section 7 concludes with the discussion. In Appendix A a rather detailed analytical and numerical study for the approximate Gaussian form of the average density of states of the TBRIM is presented while Appendices B and C deal with the specific issues of weakly excited initial states of the TBRIM, where it is difficult to obtain clear relaxation rates, and initial states with negative temperatures.

2 TBRIM construction and properties

As in Ref. [34] we consider the TBRIM [22] with M one-particle orbitals and $0 \leq L \leq M$ spinless fermions with the Hamiltonian:

$$H_I = \frac{1}{\sqrt{M}} \sum_{k=1}^M v_k c_k^\dagger c_k + \frac{4}{\sqrt{2M^3}} \sum_{i < j, k < l} J_{ij,kl} c_i^\dagger c_j^\dagger c_l c_k \quad (2)$$

where c_k^\dagger, c_k are fermion operators for the M orbitals satisfying the usual anticommutation relations. Here v_k ($J_{ij,kl}$) are real Gaussian random variables with zero mean and variance $\langle v_k^2 \rangle = V^2$ ($\langle J_{ij,kl}^2 \rangle = J^2(1 + \delta_{ik}\delta_{jl})$) such that the non-interacting orbital one-particle energies are given by $\epsilon_k = v_k/\sqrt{M}$. The variance of the interaction matrix elements is chosen such they correspond to a GOE-matrix (Gaussian orthogonal ensemble) of size $M_2 \times M_2$ with $M_2 = M(M-1)/2$. The number of nonzero elements for a column (or row) of H_I is $K = 1 + L(M-L) + L(L-1)(M-L)(M-L-1)/4$ [22, 29].

As shown in Appendix A the density of states (DOS) of the TBRIM Hamiltonian (2) is approximately Gaussian

$$\rho(E) \approx \frac{d}{\sqrt{2\pi\sigma^2}} \exp\left(-\frac{E^2}{2\sigma^2}\right) \quad , \quad \sigma = \sqrt{\frac{L(M-L)}{M(M-1)}} V_{\text{eff}} \quad (3)$$

which is normalized to $d = M!/(L!(M-L)!)$ being the dimensionality of the Hilbert space for M orbitals and L particles and

$$V_{\text{eff}} = \sqrt{V^2 + a(M, L) J^2} \quad (4)$$

is a rescaled effective energy scale taking into account the increase of σ due to finite values of J . The coefficient $a(M, L)$ is computed in Appendix A from the average of $\langle \text{Tr}(H_I^2) \rangle$ with the result :

$$a(M, L) = \frac{2(M-1)(L-1)}{M^2} \left(\frac{4}{M-L} + M - L + 3 \right). \quad (5)$$

The expression (3) fits numerically quite well the DOS for sufficiently large values of M and L and even in the SYK-case, i.e. when $J \neq 0$ but $V = 0$, it is quite accurate. The corresponding average many body level spacing (at the band center) is $\Delta_{\text{MB}} = \sqrt{2\pi}\sigma/d$. For later use we also define an effective rescaled average one-particle level spacing by $\Delta_1 = \sqrt{2\pi}V_{\text{eff}}/M^{3/2}$. At $J \ll V$ we have $V_{\text{eff}} \approx V$ and Δ_1 is just the average distance of the one-particle energies ϵ_k (in the band center). Thus the effective dimensionless conductance of our TBRIM (see [22]) is $g \approx \Delta_1/U_s \approx \sqrt{\pi}V_{\text{eff}}/2J \approx V/J \gg 1$ for $J \ll V$ and $g \approx 1$ for $J \gg V$ at $M \approx L/2$ ($U_s = 2\sqrt{2}J/M^{3/2}$ is an effective interaction strength).

Since we are using only a small number of statistical realizations, we have chosen realizations of v_k such that exactly $\sum_k v_k = 0$ and $\sum_k \epsilon_k^2 = (1/M) \sum_k v_k^2 = V^2$.

We have numerically diagonalized H_I and done further numerical computations described below for the cases $M = 12$, $M = 14$ and $M = 16$ with $L = M/2 - 1 \approx M/2$. In this work we only show the results for the case of largest matrix size $M = 16$ and $L = 7$ corresponding to $d = 11440$ (for this case the coefficient in (4) and (5) is just $a(16, 7) = 8.75$ and the number of nonzero matrix elements per row/column of H_I is $K = 820$). Unless stated otherwise, all results presented below, especially in the figures apply to this case. We have, however, verified that the physical interpretation of the results also apply to the cases of smaller matrix size (with some restrictions concerning reduced times scales for the long time behavior, more limited parameter range etc.). We present the results for one specific disorder realization but we checked that, apart from fluctuations, the results remain stable for other realizations.

First we diagonalize numerically one realization of H_I for $M = 16$, $L = 7$, $V = \sqrt{14} \approx 3.74166$, various values of J or the SYK-case (i.e. $V = 0$, $J = 1$). Similar to [34] we determine for each many body eigenstate the occupation numbers $n_k = \langle c_k^\dagger c_k \rangle$ with the corresponding fermion entropy [30] :

$$S = - \sum_{k=1}^M \left(n_k \ln n_k + (1 - n_k) \ln(1 - n_k) \right) \quad (6)$$

and the effective one-particle total energy

$$E_{1p} = \sum_{k=1}^M \epsilon_k n_k \quad (7)$$

based on the assumption on non- or weakly-interacting fermions. These energies are rather close to the exact many body energies $E_{\text{ex}} \approx E_{1p}$ provided $J \ll V$.

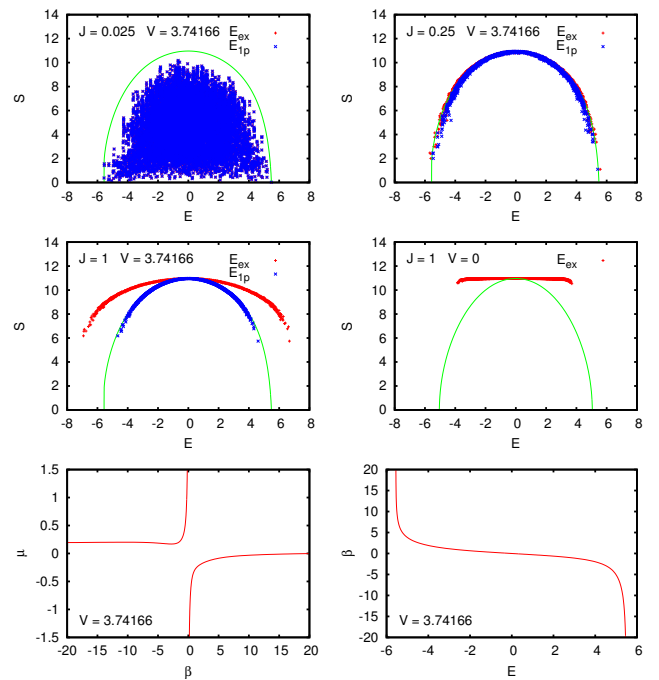


Fig. 1. (color online) *Top and center panels:* Dependence of the fermion entropy S given by (6) on the effective one-particle total energy E_{1p} defined in (7) (blue cross symbols) and the exact many body energy E_{ex} (red plus symbols). The green curve shows the theoretical Fermi-Dirac thermalization ansatz (8) as explained in the text. All panels correspond to $M = 16$ orbitals, $L = 7$ particles and Hamiltonian matrix size $d = 11440$. Both top and center left panels correspond to $V = \sqrt{14} \approx 3.74166$ and $J = 0.025$ (top left), $J = 0.25$ (top right) and $J = 1$ (center left). Center right panel corresponds to the SYK case at $V = 0$ and $J = 1$ with the green curve computed from a model of equidistant one-particle energies of non-interacting fermions. *Bottom panels:* Dependence of the inverse temperature $\beta = 1/T$ on energy E (bottom right panel) and chemical potential μ on β (bottom left panel) corresponding to the Fermi-Dirac ansatz for the set of one-particle energies ϵ_k used for the chosen realization of H_I at $V = \sqrt{14} \approx 3.74166$.

In Fig. 1 we compare the dependence of S on both energy scales with the theoretical fermionic behavior where n_k in (6) is replaced by the usual thermal Fermi-Dirac distribution (or ansatz) over one-particle orbitals [30]:

$$n_k = 1/(1 + \exp[\beta(\epsilon_k - \mu)]) , \quad \beta = 1/T \quad (8)$$

with the inverse temperature β and chemical potential μ determined by the implicit conditions (7) and $L = \sum_k n_k$ with the given set of diagonal one-particle energies ϵ_k . For the SYK case with $V = 0$ and $J = 1$ we choose for the “theoretical” curve the case of one-particles energies equidistant values ϵ_k such that $\sum_k \epsilon_k = 0$ and $\sum_k \epsilon_k^2 = V_{\text{eff}}^2$ with the effective rescaled energy scale (4) at $V = 0$ and $J = 1$ (a similar procedure was used in [34] for this SYK case).

At $V = \sqrt{14} \approx 3.74166$ one can observe in Fig. 1 the onset of thermalization with increasing interaction

strength J . At very weak interaction $J = 0.025$ the entropy is typically below the theoretical behavior indicating that the system is not thermalized. We can also mention that for this case the level spacing distribution of H_I does not obey the Wigner surmise (for the GOE case) and is closer to the Poisson distribution (with some small level-repulsion for very short energy differences). At $J = 0.25$ (this value corresponds to the case $J = 1$ in [34] due to a difference in the normalization) the system is well thermalized but the interaction is still sufficiently low so that $E_{1p} \approx E_{\text{ex}}$. Here and also for larger values of J the level spacing distribution clearly corresponds to the Wigner surmise (this was also seen in [34] and we do not show these data here). Thus at $J = 0.25$ we have onset of the dynamical thermalization induced by weak many-body interactions. At $J = 1$ the data points for E_{1p} coincide very well with the theoretical fermionic curve confirming the onset of dynamical thermalization induced by interactions. However, here due the stronger interaction values the ratio E_{ex}/E_{1p} is considerably larger than unity.

For the SYK case $V = 0$, $J = 1$ the entropy is close to its maximal value $S \approx 11$ for nearly all eigenstates and the theoretical model of equidistant one-particle energies is not confirmed. This value of S is actually consistent with $n_k \approx 0.5$ for all orbitals k which gives due (6) $S \approx 16 \ln(2) \approx 11.1$. For the SYK case the numerical level spacing distribution also corresponds to the Wigner surmise.

The results of this Section show that at moderate interactions with $g \ll 1$ the DTC is well working (e.g. $J = 0.25$, $V = \sqrt{14}$, $g \approx 15$) and the dependence $S(E)$ is well described by the thermal Fermi-Dirac distribution (8). Of course, at very small interactions (e.g. $J = 0.025$, $V = \sqrt{14}$, $g \approx 150$) the DTC is not valid in qualitative agreement with the Åberg criterion (1). Here we do not investigate the exact numerical values for the Åberg criterion since our main aim is the investigation of the interaction of a qubit with the TBRIM in the regimes of a thermalized quantum dot (e.g. $g \approx 15$) or SYK black hole (e.g. $g \approx 1$, $V = 0$, $J = 1$). As discussed in [34] the question about thermal description of quantum chaos via effective hidden modes in the SYK regime remains open.

3 Qubit interacting with TBRIM

In order to study the decoherence of one qubit coupled to the fermionic system described by the TBRIM Hamiltonian H_I defined in (2) we consider the total Hamiltonian

$$H = \delta \cdot \sigma_x + \varepsilon \frac{V_{\text{eff}}}{V_0} \sigma_z \sum_{k=1}^{M-1} (c_k^\dagger c_{k+1} + c_{k+1}^\dagger c_k) + H_I \quad (9)$$

where σ_x and σ_z are the usual Pauli matrices in qubit space and δ is (half) the unperturbed energy separation of the two qubit levels introducing Rabi oscillations with frequency $\omega_R = 2\delta$. We typically choose $\delta = \Delta_1/2$ (or a simple multiple of this) with Δ_1 being the effective rescaled

one-particle level spacing given above in terms of the effective energy scale V_{eff} . In (9) we have chosen the orbital indices k such that the one-particle energies are ordered, i.e. $\epsilon_{k+1} > \epsilon_k$, implying that the qubit-fermion coupling term creates transitions between adjacent orbitals with approximate energy difference $\sim \Delta_1$. The quantity ε is the coupling parameter which will take various values in the interval $0.005 \leq \varepsilon \leq 1$ and the ratio V_{eff}/V_0 (with $V_0 = \sqrt{14}$) ensures that at different values of V and J the coupling parameter is measured in units of the overall bandwidth $\sigma \sim V_{\text{eff}}$ such that results at different values of V and J at same ε are indeed comparable. We mention that the Hamiltonian (9) is similar in structure to the Hamiltonian studied in Ref. [8] where the qubit was coupled to a quantum kicked rotor model. As already mentioned we present below results for $M = 16$ orbitals and $L = 7$ particles corresponding to a combined qubit-fermion Hilbert space dimension of 22880 but we have also verified the smaller cases at $M = 12$ or $M = 14$ with $L = M/2 - 1$ obtaining there similar results.

Explicitly, we compute numerically the exact time evolution of a state $|\psi_m(t)\rangle = \exp(-iHt) |\psi_m(0)\rangle$ with the initial vector

$$|\psi_m(0)\rangle = |\phi_m\rangle (|0\rangle + 2|1\rangle)/\sqrt{5} \quad (10)$$

where $|\phi_m\rangle$ is an exact eigenstate of H_I at level number m with many body energy E_m , i.e. $H_I |\phi_m\rangle = E_m |\phi_m\rangle$, and $|0\rangle$, $|1\rangle$ denote the two qubit states with bottom and upper energies. The time evolution operator $\exp(-iHt)$ is computed exactly by diagonalizing H and expressing the matrix exponential using the exact eigenvalues and eigenvectors of H . For $M = 16$ and $L = 7$ this corresponds to a numerical diagonalization in the combined fermion-qubit Hilbert space of dimension 22880. As in Ref. [8] we determine the 2×2 density matrix $\rho_{ij}(t)$, $i, j = 0, 1$ from the partial trace over the fermionic states by: $\rho_{ij}(t) = \langle i | \text{Tr}_{\text{ferm.}} (|\psi_m(t)\rangle \langle \psi_m(t)|) | j \rangle$. In absence of qubit-fermion coupling, i.e. $\varepsilon = 0$, the density matrix $\rho(t)$ does not depend on the choice of $|\phi_m\rangle$ and a simple standard calculation gives the result:

$$\rho_{11}(t) = 1 - \rho_{00}(t) = \frac{1}{2} + \frac{3}{10} \cos(\omega_R t) \quad , \quad (11)$$

$$\rho_{01}(t) = \rho_{10}^*(t) = \frac{2}{5} + \frac{3}{10} i \sin(\omega_R t) \quad , \quad (12)$$

$$\Rightarrow |\rho_{01}(t)| = \frac{1}{2} \left(\frac{41}{50} - \frac{9}{50} \cos(2\omega_R t) \right)^{1/2} \quad , \quad (13)$$

where $\omega_R = 2\delta$ is the Rabi frequency.

For practical reasons we compute the density matrix $\rho(t)$ at $t = \tau \Delta t$ with integer values of τ and the elementary time unit $\Delta t = 1/(\Delta_1 M)$ where Δ_1 is the rescaled effective one-body level spacing. This time step corresponds roughly to the inverse one-particle band-width and represents the shortest quantum time scale in the system. We consider the maximal time value $t_{\text{max}} = (d/2) \Delta t = 5720 \Delta t = \sqrt{\frac{L(M-L)}{4(M-1)}} t_H \approx t_H$ with $L \approx M/2$ and $t_H = 1/\Delta_{\text{MB}}$ being the Heisenberg time.

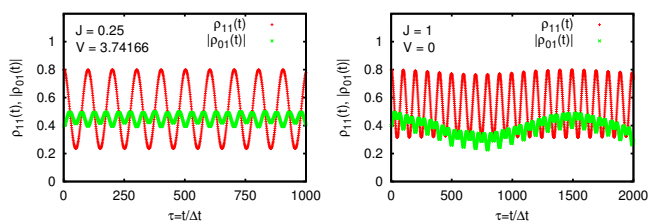


Fig. 2. Time dependence of $\rho_{11}(t)$ (red plus symbols) and $|\rho_{01}(t)|$ (green crosses) for the initial state being the ground state of H_I with the level number $m = 0$ and qubit state (10) for $V = 3.74166$, $J = 0.25$ ($V = 0$, $J = 1$) in left (right) panel at coupling strength $\varepsilon = 0.01$. The time is measured in units of $\Delta t = 1/(\Delta_1 M)$ where Δ_1 is the rescaled effective one-body level spacing defined in the text.

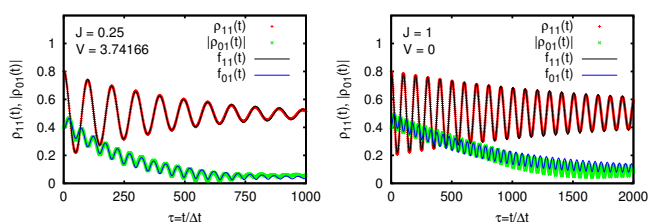


Fig. 3. (color online) As in Fig. 2 but for level number $m = 5720$ of the initial state (10) corresponding to an energy in the center of the spectrum of H_I . The fit functions $f_{11}(t)$ (thin black line) to approximate $\rho_{11}(t)$ and $f_{01}(t)$ (thin blue line) to approximate $|\rho_{01}(t)|$ are given by (14) and (15) with the fit parameters : $A_1 = 0.49593 \pm 0.00005$, $B_1 = 0.3070 \pm 0.0002$, $\Gamma_1 = 0.002195 \pm 0.000003$, $\omega_1 = 0.063423 \pm 0.000003$, $\alpha_1 = 6.2492 \pm 0.0006$ and $A_2 = 0.0063 \pm 0.0001$, $\tilde{B}_2 = 0.194 \pm 0.001$, $\tilde{\Gamma}_2 = 0.00435 \pm 0.00004$, $\omega_2 = 0.12641 \pm 0.00004$, $\alpha_2 = 3.232 \pm 0.007$, $B_2 = 0.800 \pm 0.001$, $\Gamma_2 = 0.00713 \pm 0.00002$ for $V = 3.74166$, $J = 0.25$ (left panel) and $A_1 = 0.5008 \pm 0.0001$, $B_1 = 0.2897 \pm 0.0004$, $\Gamma_1 = 0.000449 \pm 0.000002$, $\omega_1 = 0.062552 \pm 0.000002$, $\alpha_1 = 6.228 \pm 0.0002$ and $A_2 = 0.0391 \pm 0.0004$, $\tilde{B}_2 = 0.172 \pm 0.002$, $\tilde{\Gamma}_2 = 0.00094 \pm 0.00002$, $\omega_2 = 0.12508 \pm 0.00002$, $\alpha_2 = 3.06 \pm 0.02$, $B_2 = 0.825 \pm 0.002$, $\Gamma_2 = 0.00209 \pm 0.00001$ for $V = 0$, $J = 1$ (right panel).

In Fig. 2 we show the time dependence of $\rho_{11}(t)$ and $|\rho_{01}(t)|$ for a weak coupling strength $\varepsilon = 0.01$, an initial state (10) with level number $m = 0$, corresponding to the ground state of H_I , and two cases for different values of V and J . For $\varepsilon = 0.01$ the dependence $\rho_{11}(t)$ is close to the analytical result (11). However for $|\rho_{01}(t)|$ the situation is more complicated with the appearance of a further frequency leading to a quasi-periodic structure. Apparently the ground state $|\phi_0\rangle$ of H_I is also weakly coupled to the next state $|\phi_1\rangle$ due to the indirect qubit-fermion coupling leading to an additional frequency. The results of Fig. 2 show that there is no qubit decoherence when it is coupled with a quantum dot or SYK system when they are in their ground state.

For higher level numbers m the situation changes and for many eigenstates $|\phi_m\rangle$ of H_I an exponential relaxation is found for $\rho_{00}(t)$ tending to the equilibrium value $1/2$

and $|\rho_{01}(t)|$ tending to a value $\sim 1/\sqrt{n}$ where n is roughly the number of eigenstates of H_I contributing in $|\psi_m(t)\rangle$. Therefore, motivated by the analytic expressions at $\varepsilon = 0$, we use the following fit functions for small values $0 < \varepsilon \ll 1$:

$$f_{11}(\tau\Delta t) = A_1 + B_1 e^{-\Gamma_1\tau} \cos(\omega_1\tau + \alpha_1) \quad , \quad (14)$$

$$f_{01}(\tau\Delta t) = \frac{1}{2} \left(A_2 + \tilde{B}_2 e^{-\tilde{\Gamma}_2\tau} \cos(\omega_2\tau + \alpha_2) + B_2 e^{-\Gamma_2\tau} \right)^{1/2} \quad , \quad (15)$$

to approximate $\rho_{11}(t)$ by $f_{11}(t)$ and $|\rho_{01}(t)|$ by $f_{01}(t)$. The parameter $\tau = t/\Delta t$ is the rescaled time in units of $\Delta t = 1/(\Delta_1 M)$ where Δ_1 is the rescaled effective one-body level spacing introduced above. These fits work very well for the two cases shown in Fig. 3 with level number $m = 5720$ (corresponding to the band center of H_I) and $\varepsilon = 0.01$. From (11), (12) and for the choice $\delta = \Delta_1$, $M = 16$ we expect that $\omega_1 = \omega_R \Delta t = 2\delta/(M\Delta_1) = 1/M = 0.0625$ and $\omega_2 = 2\omega_1 = 0.125$ which is indeed well confirmed by the fits shown in Fig. 3.

For larger values of the coupling strength $\varepsilon \geq 0.1$ the fits with the oscillatory terms do not work very well and have to be simplified to simple exponential fits, i.e. by omitting the term $\sim \tilde{B}_2$ in (15) or replacing $\cos(\omega_1\tau + \alpha_1) \rightarrow 1$ in (14). In Appendix B we discuss certain cases, with low values of the level number m of the initial state (10) where the fit procedure is also problematic. However, in global the fits of the relaxation of the density matrix components work well and allow to determine the dependence of the relaxation rates Γ_1, Γ_2 on system parameters.

4 Qubit relaxation rates

4.1 Dependence on coupling strength

The relaxation rates are computed by the methods described in the previous Section. Here we analyze the dependence of these rates on system parameters. We note that according to usual cases of superconducting qubit relaxation [5,6,7,8] the rate Γ_2 describes the dephasing of qubit while Γ_1 describes the population relaxation.

The obtained dependence of Γ_1 on the qubit coupling strength ε is shown in Fig. 4 for the initial state $m = 5720$ taken in the middle of the total energy band and the TBRIM values $J = 0.15, 0.25, 1$ at $V = 3.74166$ ($V_{\text{eff}}/V_0 = 1.0070, 1.0193, 1.2747$ and $\Delta_1 = 0.1475, 0.1494, 0.1868$ respectively) corresponding to the quantum dot regime and $J = 1$ at $V = 0$ ($V_{\text{eff}}/V_0 = 0.7905$, $\Delta_1 = 0.1158$) corresponding to the SYK black hole regime. For small coupling $\varepsilon < 0.1$ the results are well described by the quadratic dependence on coupling, typical for the Fermi golden rule regime:

$$\Gamma_1 = C_1 \varepsilon^2 \quad . \quad (16)$$

The fit value of the exponent is $p = 2.00 \pm 0.02$ being compatible with the quadratic dependence.

The dimensionless constant C_1 in (16) is practically independent of J (at fixed $V = \sqrt{14}$) when the system is in the regime of dynamical thermalization being $C_1 \approx 23$ for $J = 0.15, 0.25$ and $C_1 \approx 8$ for $J = 1$. For the SYK case we find $C_1 = 4.6 \pm 0.3$ at $J = 1, V = 0$. We consider that this variation of C_1 is not significant since it changes only by a factor 5 while J^2 is changed by a factor 44 and in addition the model is changed from quantum dot to SYK regime. At such changes the total energy band width is also changed by a factor 2 (see Fig. 1) but we remind that due to the definition of the model and parameters in Sections 2 and 3 both ε and the relaxation rates are measured in units of effective energy (or inverse time) scales that take into account the modification of total energy band width due to different values of V and J . We note that the dependence (16) was also found for the dynamical relaxation of a qubit coupled to a deterministic detector described by the quantum Chirikov standard map [8] with $C_1 \approx 0.5$ corresponding to regime of the phase damping noise channel [2, 8]. Here we obtain C_1 being by a factor 10 larger but in our model (9) the qubit is coupled with several TBRIM states and we assume that this is the reason for the increase of C_1 .

For $\varepsilon > \varepsilon_c \approx 0.1$ we obtain a decrease of the relaxation rate described by the dependence

$$\Gamma_1 = C_1 \varepsilon^p, \quad p = -1.15 \pm 0.02 \quad (17)$$

with $C_1 \approx 0.002$. As in [8] we attribute this decrease of Γ_1 with increase of ε to the quantum Zeno effect [49, 50]: repeated measurements produced by a coupled detector, represented by TBRIM in the regime of quantum chaos, reduce the relaxation rate. In the so called ohmic relaxation regime it is expected that $\Gamma_1 \sim \delta^2/\Gamma_2 \sim B\delta^2/\varepsilon^2$ [6, 8] (here $\delta = \Delta_1/2$). For the model of quantum chaos detector it was found that $B \approx 2.7$ [8]. Instead, here we find that the exponent $|p| = 1.15 \pm 0.02 \approx 1$ being significantly different. We attribute this difference to the fact that in TBRIM the qubit is coupled to many one-particle states represented by a sum over k in (9). For the numerical value $C_1 \approx 0.002$ we find that it is still approximately given by the relation $C_1 \approx B\delta^2$ with $B \approx 0.4$ being smaller than those in [8]. A surprising feature of the obtained quantum Zeno regime is that here Γ_1 is practically independent of parameter choice presented in Fig. 4 corresponding to DTC for the quantum dot and SYK quantum chaos regimes.

The transition between the Fermi golden mean regime ($\Gamma_1 \propto \varepsilon^2$) and the quantum Zeno regime ($\Gamma_1 \propto 1/\varepsilon$) takes place at $\varepsilon_c \approx 0.07 - 1$. This corresponds to the relaxation rate $\Gamma_c = \Gamma_1(\varepsilon_c) \approx 0.05$ which remains practically the same for all parameter regimes presented in Fig. 4. According to the results and arguments presented in [8, 51, 52] it is expected that Γ_c is given by the Lyapunov exponent Λ of an underlined classical dynamics of the detector coupled to qubit. Indeed, this was the case for the dynamical detector considered in [8], however, for the TBRIM it is more difficult to establish what is the Lyapunov exponent of the corresponding classical TBRIM dynamics. It would be possible to expect that Γ_c can be related to the

Breit-Wigner width $\Gamma \sim J^2 \rho_c$ appearing in the TBRIM in the Fermi golden rule for the transition between directly coupled states with the density ρ_c [53]. However, the independence of Γ_c of system parameters presented in Fig. 4 excludes this expectation.

We make the conjecture that for given parameters Γ_c is determined by an effective time T_c of spreading over the network of exponentially large size d ($\ln d \sim M$ at large M, L values) with a very small number of links (nonzero transition matrix elements): $N_l = K = 820 \ll d = 11440$ (for $M = 16$ and $L = 7$). Such a network is similar to the small-world networks appearing in many cases of social relations [54, 55]. It is known that a very rapid spreading takes place on such networks for classical [55] and quantum spreading [56] with a time scale T_c being only logarithmic in system size d (effect of *six degrees of separation* described in [54, 55]). Thus about six transitions (links) are required to connect on average any pair of nodes on such networks (for the Facebook network there is only four degrees of separation [57]). For typical networks like Wikipedia or WWW of universities there are only about $N_\ell \sim 10 - 20$ nonzero links per row/column in the full matrix of the network of size $d \sim 10^6$ [58].

In the TBRIM case we have a much larger number of links per row/column and thus we expect that only about 2-4 transitions are sufficient to connect any two nodes (levels) of the system. Due to this we can expect that in this quantum small-world regime we have $\Gamma_c \sim C_d \Delta_1$ with a numerical constant $C_d \approx 0.5$. The proportionality $\Gamma_c \propto \Delta_1$ appears since Δ_1 plays a role of oscillator frequency (as for an oscillator) determining the time scale in the regime of explosive spreading over network, C_d is inversely proportional to the degree of separation of the network which is of the order of 2-4 transitions for TBRIM since the number of links per column is much larger than for Wikipedia or Facebook networks. Thus we assume that this kind of explosive spreading, already discussed in [56], is at the origin of the independence of Γ_c of system parameters (for the range visible in Fig. 4). We note that this kind of explosive spreading, with exponentially many states populated in a finite time, was also observed for the emergence of quantum chaos in a quantum computer core [59] (see e.g. Fig. 6 there).

The dependence of the dephasing rate Γ_2 on the coupling strength ε is shown in Fig. 5 for the parameters considered in Fig. 4. In agreement with the usual expectations [6, 8] we find

$$\Gamma_2 = C_2 \varepsilon^2, \quad C_2 = 24 \pm 8. \quad (18)$$

Indeed, the numerical fit gives the exponent $p = 2.02 \pm 0.09$ being very close to the Fermi golden rule value $p = 2$. For the range $\varepsilon < \varepsilon_c \approx 0.7$ we have the approximate relation $\Gamma_1 \approx \Gamma_2$ as it was also found in [8] corresponding to the general results of Ref. [6]. We note that the fit results give for the other exponential decay rate $\tilde{\Gamma}_2$ of the oscillatory term in (12) (see full color circles in Fig. 5) comparable values and parameter dependence as for Γ_2 .

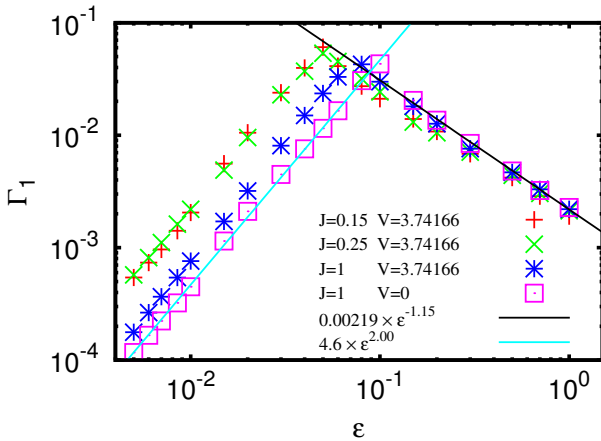


Fig. 4. (color online) Dependence of the relaxation rate Γ_1 on the coupling strength ε at level number $m = 5720$ for the initial state (10) for $V = 3.74166$, $J = 0.15$ (red plus symbols), $J = 0.25$ (green crosses), $J = 1$ (dark blue stars) and $V = 0$, $J = 1$ (pink squares) in a double logarithmic representation. The two lines correspond to the power law fits $\Gamma_1 = C_1 \varepsilon^p$ for $V = 0$, $J = 1$ with $C_1 = 4.6 \pm 0.3$, $p = 2.00 \pm 0.02$ for $\varepsilon \leq 0.1$ (light blue line) and $C_1 = 0.00219 \pm 0.00006$, $p = -1.15 \pm 0.02$ for $\varepsilon > 0.1$ (black line).

4.2 Dependence on excitation level number

The dependence of decay rates on the initial eigenvalue number m (with eigenstate energy $E_{\text{ex}}(m)$) is shown for Γ_1 in Fig. 6 and Γ_2 in Fig. 7. All data are given for a weak qubit coupling $\varepsilon = 0.01$ corresponding to the Fermi golden rule regime in Fig. 4. The independence of m is surprising since we know that the density of coupled states for effectively interacting electrons excited above the Fermi level ε_F on energy $\varepsilon \approx T \ll \varepsilon_F$ growth with energy as $\rho_c \approx T^3/\Delta_1^4$ (number of effectively interacting electrons is $\delta n \sim T/\Delta_1$ and the effective density of interacting two-particle states is $\rho_{2,\text{eff}} \sim T/\Delta_1$ with $\rho_c \sim \rho_{2,\text{eff}}(\delta n)^2$) and the interaction induced transition rate also grows with energy as $\Gamma_c \sim J^2 \rho_c \sim J^2 T^3/\Delta_1^4$ [19, 22]. Thus one could expect an increase of Γ_1, Γ_2 with an increase of m . The results presented in Figs. 6, 7 clearly show no increase with m for the range $500 \leq m \leq 5720$, for the range $100 \leq m < 500$ there is also no increase with m but the data is more fluctuating. These fluctuations become even stronger for the range $0 \leq m < 100$ so that the fits of relaxation decay in this range become not reliable (this is discussed in detail in Appendix Section B). The increase of fluctuations at low excitation numbers m is natural since for lower m values we have a decrease of number of states effectively coupled to the qubit. We note that the values of $\tilde{\Gamma}_2$, shown by full circles in Fig. 7, show a similar behavior as Γ_2 (with somewhat larger fluctuations at low m values since the corresponding fit (15) is more sensitive to errors).

Thus even if the variation of m is rather large (factor 10 or 50) the variation of Γ_1, Γ_2 remains in the same range as in Figs. 4, 5 being restricted approximately by a factor

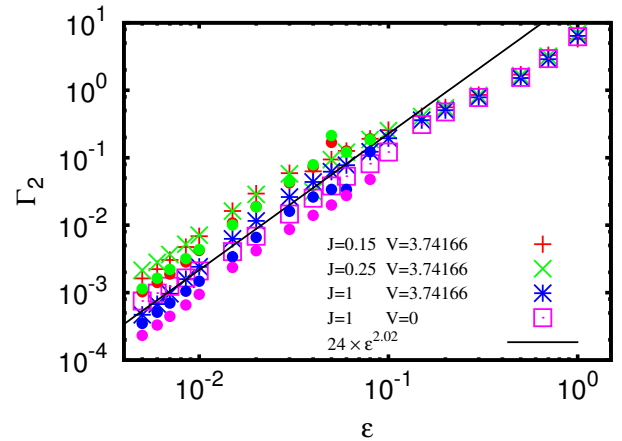


Fig. 5. (color online) Dependence of the relaxation rate Γ_2 obtained from the fit (15) on the coupling strength ε at level number $m = 5720$ for the initial state (10) for $V = 3.74166$, $J = 0.15$ (red plus symbols), $J = 0.25$ (green crosses), $J = 1$ (dark blue stars) and $V = 0$, $J = 1$ (pink squares) in a double logarithmic representation. The black line corresponds to the power law fit $\Gamma_2 = C_2 \varepsilon^p$ for the case $V = 3.74166$, $J = 1$ with $C_2 = 24 \pm 8$, $p = 2.02 \pm 0.09$ and fit range $\varepsilon \leq 0.1$. The data points with small full circles correspond to the relaxation rate $\tilde{\Gamma}_2$ of the oscillatory term for $\varepsilon < 0.1$ in (15) (same colors as other data points for different cases of V and J). For $\varepsilon \geq 0.1$ the relaxation rate Γ_2 is obtained from a simplified exponential fit without oscillatory term.

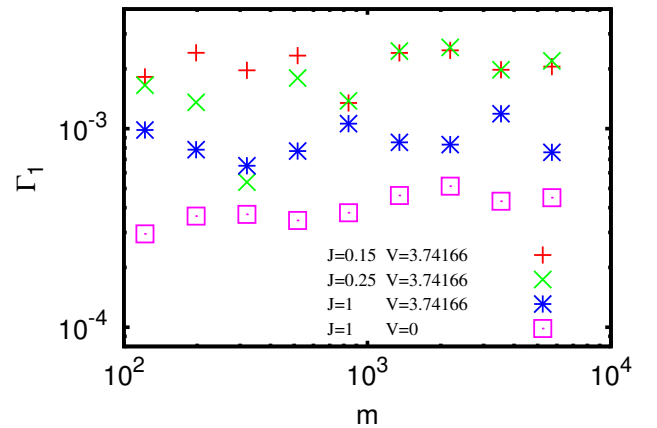


Fig. 6. (color online) Dependence of the relaxation rate Γ_1 on the level number m used for the initial state (10) at coupling strength $\varepsilon = 0.01$ for $V = 3.74166$, $J = 0.15$ (red plus symbols), $J = 0.25$ (green crosses), $J = 1$ (dark blue stars) and $V = 0$, $J = 1$ (pink squares) in a double logarithmic representation.

5. We explain this independence of m in the same manner as in previously arguing that for $m > 100$ the transitions between non-interacting many-body states proceed in an explosive spreading typical on small-world networks in a regime $\Gamma_1 \approx \Gamma_2 \sim 30\Delta_1 \gg \Delta_1$. In fact for $m \approx 100$, $J = 0.15$ we find $\delta E \approx T^2/\Delta_1 \approx 1.4$ with $\Delta_1 = 0.1475$ that

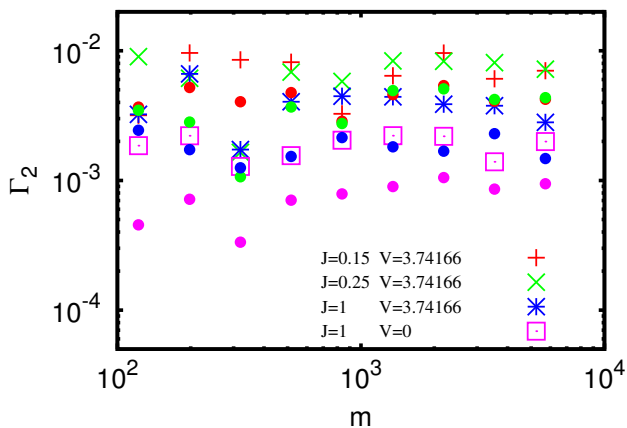


Fig. 7. (color online) Dependence of the relaxation rate Γ_2 obtained from the fit (15) on the level number m used for the initial state (10) at coupling strength $\varepsilon = 0.01$ for $V = 3.74166$, $J = 0.15$ (red plus symbols), $J = 0.25$ (green crosses), $J = 1$ (dark blue stars) and $V = 0$, $J = 1$ (pink squares) in a double logarithmic representation. The data points with small full circles correspond to the relaxation rate \tilde{T}_2 of the oscillatory term in (15) (same colors as other data points for different cases of V and J).

gives $T \approx 0.45$ (see Fig. 1) and from above estimates we obtain $\Gamma_c/\Delta_1 \approx 30$. This ratio becomes even larger for other parameters of Figs. 4, 6.

5 TBRIM as a quantum small-world network

Above we proposed an analogy between the TBRIM and a quantum small-world networks studied in [56,60], tracing parallels with the small-world networks in social relations [54,55]. On a first glance this analogy may look to be strange since for TBRIM the number of nonzero matrix elements per row/column of the Hamiltonian matrix is fixed being K while the small-world networks are characterized by a broader distribution of links [55]. However, for the TBRIM the physical relevant quantity is not the formal number of nonzero elements but the number of effectively directly coupled states. As was discussed above and in [19,22] the density and number of such states depends on energy (this is especially visible in proximity of the Fermi energy). According to quantum perturbation theory we need to count only transitions for which the transition matrix element is at least comparable to the energy detuning between the states involved in the transition. For the states with large energy detunings the effective probabilities (weights) of the transitions become small and their influence can be neglected, at least in a first approximation.

Therefore we construct from the TBRIM Hamiltonian H_I defined in (2) an effective (symmetric undirected) network where two many-body states i and j are coupled by a link if the condition $|(H_I)_{ij}| > C|(H_I)_{ii} - (H_I)_{jj}|$ is met where C is a parameter of order unity which we either

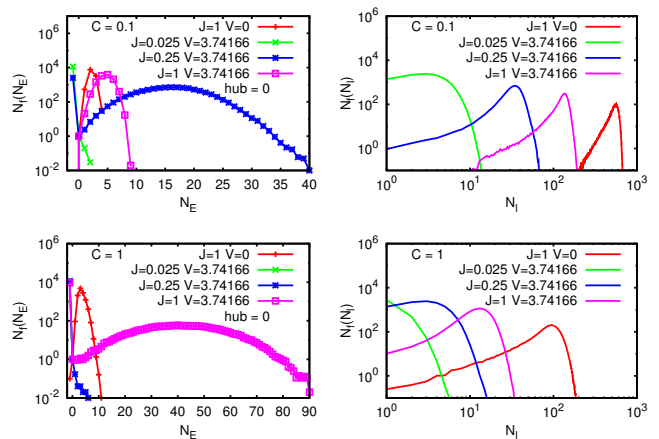


Fig. 8. (color online) Frequency distributions $N_f(N_i)$ of link number N_i per node (right panels) and $N_f(N_E)$ of Erdős number N_E (left panels) for an effective network constructed from H_I where states/nodes i and j are connected by a link if the condition $|(H_I)_{ij}| > C|(H_I)_{ii} - (H_I)_{jj}|$ with the cut value $C = 0.1$ (top panels) or $C = 1$ (bottom panels) is met. The Erdős number N_E of a node represents the minimal number of links necessary to connect indirectly this node via other intermediate nodes to the hub = 0 corresponding to the many-body state where first 7 out of 16 orbitals are occupied. The hub itself has $N_E = 0$ and the value $N_E = -1$ indicates that a node cannot be indirectly connected to the hub. Color of curves/data points is red (SYK, $V = 0$, $J = 1$), green ($V = \sqrt{14}$, $J = 0.025$), blue ($V = \sqrt{14}$, $J = 0.25$) and pink ($V = \sqrt{14}$, $J = 1$). For these four cases respectively the mean and the width of the distribution of N_i are: 532 ± 61 , 3.35 ± 1.87 , 33.7 ± 7.3 , 129 ± 20 ($C = 0.1$, top right panel) and 91.8 ± 25.2 , 0.346 ± 0.586 , 3.36 ± 1.89 , 13.4 ± 4.09 ($C = 1$, bottom right panel); also the mean and the width of the distribution of N_E (not counting $N_E = -1$ cases) are: 2.24 ± 0.53 , 0.211 ± 0.464 , 16.1 ± 4.86 , 4.63 ± 1.12 ($C = 0.1$, top left panel) and 3.40 ± 1.09 , 0 ± 0 , 0.469 ± 1.10 , 41.2 ± 13.7 ($C = 1$, bottom left panel). In bottom left panel the green curve is completely hidden by the blue curve and contains only two values $N_f(-1) = 11439$ and $N_f(0) = 1$ meaning that the hub is not connected to any other node. All curves were obtained from an average of 100 different random realizations of H_I for $M = 16$, $L = 7$ and $d = 11440$. The vertical axis represents the number N_f of nodes having the link number N_i (right panels) or having the Erdős number N_E (left panels).

choose $C = 0.1$ or $C = 1$. This can be considered as a numerical selection following the Åberg criterion [19,22]. A similar procedure has been considered in [61] for spin chains. We emphasize that the diagonal matrix elements $(H_I)_{ii}$ are constituted of two contributions: the first term in (2) given by the sum of energies of occupied orbitals and certain non-vanishing diagonal contributions from the interaction which have, according to the discussion in Appendix A, a variance which is $L(L-1)$ larger than the variance of the non-diagonal interaction matrix elements (for the case where two occupied orbitals differ between the two states). For the limit $J \ll V$ the diagonal matrix elements are of course dominated by the orbital energy

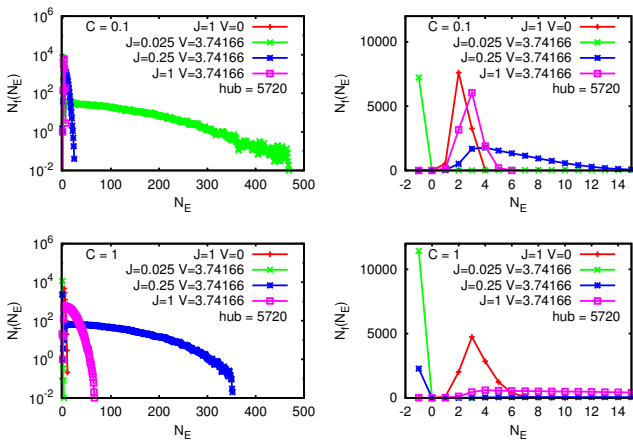


Fig. 9. (color online) Frequency distribution $N_f(N_E)$ of Erdős number N_E for the same effective network of Fig. 8 for the hub = 5720 corresponding to the many-body state where orbitals: 3, 4, 8, 9, 12, 14, 15 out of 16 orbitals are occupied. The signification of N_E is as in Fig. 8 and the value of $N_E = -1$ corresponds to the case of nodes not connected to the hub. Top (bottom) panels correspond to the cut value $C = 0.1$ ($C = 1$). Left panels correspond to the range $-2 \leq N_E \leq 500$ and a logarithmic representation for $N_f(N_E)$ and right panels correspond to a zoomed range $-2 \leq N_E \leq 15$ and normal representation for $N_f(N_E)$. Color of curves/data points is red (SYK, $V = 0$, $J = 1$), green ($V = \sqrt{14}$, $J = 0.025$), blue ($V = \sqrt{14}$, $J = 0.25$) and pink ($V = \sqrt{14}$, $J = 1$). For these four cases respectively the mean and the width of the distribution of N_E (not counting $N_E = -1$ cases) are: 2.24 ± 0.53 , 96.5 ± 74.9 , 6.22 ± 3.03 , 2.90 ± 0.74 ($C = 0.1$, top panels) and 3.42 ± 1.10 , 0.371 ± 0.622 , 91.7 ± 64.7 , 15.1 ± 9.5 ($C = 1$, bottom panels). All curves were obtained from an average over the same 100 different random realizations of H_I ($M = 16$, $L = 7$, $d = 11440$) used in Fig. 8.

contribution but even for the SYK case with vanishing orbital energies ($V = 0$, $J = 1$) the diagonal terms have a considerable size due to the diagonal interactions.

Using this kind of network model we determine the frequency distribution $N_f(N_l)$ of number of links per node N_l for the four cases $V = 0$, $J = 1$ (SYK case with strongest interactions and quantum chaos), $V = \sqrt{14}$, $J = 0.025$ (weak interactions without dynamical thermalization), $V = \sqrt{14}$, $J = 0.25$ (moderate interactions with dynamical thermalization) and $V = \sqrt{14}$, $J = 1$ (strong interactions with dynamical thermalization). Furthermore we choose our standard parameters $L = 7$, $M = 16$ giving a matrix dimension $d = 11440$ of H_I and the number of non-zero couplings elements per state $K = 820$ which is an obvious upper bound for N_l . As can be seen in Fig. 8 the frequency distribution of N_l is not a power law and not scale free. Essentially the criterion in terms of diagonal energy differences implies that the typical link number N_l is a certain fraction of K which does not fluctuate too strongly for different initial states. However, this fraction is smallest for $V = \sqrt{14}$, $J = 0.025$ with a maximal value $N_{f,\max} = 16$ (if $C = 0.1$) or 7 (if $C = 1$) and largest for the

SYK case $V = 0$, $J = 1$ with $N_{f,\max} = 687$ (if $C = 0.1$) or 217 (if $C = 1$). According to Fig. 8 the frequency distribution of N_l provides largest values for the case of strongest coupling (SYK, $V = 0$, $J = 1$) and smallest values for the case of weakest coupling ($V = \sqrt{14}$, $J = 0.025$). The choice $C = 1$ as compared to $C = 0.1$ provides a general shift to smaller values. Actually, for $V = \sqrt{14}$ the case $C = 1$, $J = 0.25$ is rather obvious since reducing the constant C by a certain factor corresponds to reducing the typical interaction couplings by the same factor. However, these two cases are not perfectly identical and the remaining small differences are due to complications from the diagonal interaction matrix elements in $(H_I)_{ii}$.

In global we see that the frequency distribution of links $N_f(N_l)$ is peaked near a certain average value that can be viewed as a broadening of the delta-function distribution of random graphs introduced by Erdős-Rényi [62], known as the Erdős-Rényi model [55]. Below we check if our quantum network possesses the small-world property typical for the social networks [54, 57, 55]

With this aim we compute a more interesting quantity which we call the Erdős number N_E . This number represents the minimal number of links necessary to connect indirectly a specific node via other intermediate nodes to a particular node called the hub.

We choose as hub two example states at index values 0 and 5720 in the many body Hilbert space of dimension $d = 11440$ (at $M = 16$ and $L = 7$). In our numerical mapping of states (i.e. the way the many-states are enumerated) the hub = 0 corresponds to the state where the the first L of the M (i.e. first 7 of 16) orbitals are occupied. Since we have chosen the orbital energies ordered with respect to the orbital index number (see text below Eq. (9)) this state corresponds to the non-interacting ground state, i.e. the Fermi sea, for the case $V > 0$ and $J = 0$. According to the Gaussian density of states this implies that typical energy differences of this state with the next excited states are rather large and therefore this hub is quite “badly” coupled to other nodes in our network model.

The other hub = 5720 corresponds roughly to a state in the middle of the non-interacting energy spectrum (for $V > 0$ and $J = 0$) and in our numerical mapping this corresponds to the state where the 7 orbitals: 3, 4, 8, 9, 12, 14, and 15 are occupied. Here the typical energy differences with respect to neighbor states are quite small.

Therefore, for the three cases with $V = \sqrt{14}$ we expect there will be a considerable difference in the connectivity between both hubs. However, for the SYK case with $V = 0$ and $J = 1$ the residual diagonal energies in H_I of these states (due to the interaction) are really fully random and both hubs are statistically expected to be equivalent and rather well connected.

The Erdős number corresponds roughly to the ergodic time scale (in units of link-iterations) for the classical stochastic dynamics induced by the network. Depending on the typical coupling strength of the network it is possible that certain or even many nodes are not at all coupled to the hub by indirect links, especially for the hub = 0

(if $V > 0$). In this case we attribute artificially the value $N_E = -1$ to such topologically separated nodes from the hub, while the hub itself has $N_E = 0$ and the remaining nodes (indirectly coupled to the hub) have values $N_E > 0$.

The frequency distribution $N_f(N_E)$ of the Erdős number N_E for hub = 0 is shown in the left panels of Fig. 8. For the SYK case (strongest coupling) the distribution is strongly peaked with typical values at ~ 2 (~ 3) for $C = 0.1$ ($C = 1$). Then with decreasing coupling (or increasing value of C) the width and mean values of the distribution increase provided there is still a sufficient fraction of nodes (indirectly) coupled to the hub. For the cases of weakest coupling $V = \sqrt{14}$, $J = 0.025$ (if $C = 0.1$) or $J \leq 0.25$ (if $C = 1$) nearly all nodes are not at all coupled to the hub as can be seen from the strong peaks at $N_E = -1$. The mean and width of the distribution of the few number of remaining nodes (eventually only the hub itself) is very small. For the two cases $V = \sqrt{14}$, $J = 0.25$ (if $C = 0.1$) or $J = 1$ (if $C = 1$) there is a large fraction of isolated nodes but there are still enough remaining nodes coupled to the hub providing a non-trivial distribution of largest values ~ 40 or ~ 90 respectively. Apart from the SYK cases only the case $V = \sqrt{14}$, $J = 1$ at $C = 0.1$ provides a strongly peaked distribution with typical value at 4.6 ± 1 .

Fig. 9 shows the frequency distribution $N_f(N_E)$ of the Erdős number N_E for the other hub = 5720. As expected the two SYK cases are very similar to the first hub = 0 of Fig. 8. However for the cases with $V = \sqrt{14}$ the connectivity is indeed “better” as compared to Fig. 8, i.e. either the typical values are smaller or there are less isolated nodes (lower or absent peaks at $N_E = -1$). Especially the two cases $J = 0.025$ (if $C = 0.1$) or $J = 0.25$ (if $C = 0$), with nearly only isolated nodes in Fig. 8, provide now a non-trivial rather large distribution for a modest fraction of non isolated nodes. Furthermore, these two cases are actually quite comparable as already discussed above for the frequency distribution of links.

The last two cases correspond to a (partial) ergodicity but only after a large number of network iterations. This observation may be related to a diffusive dynamics in energy space where it takes some time to explore different energy layers such that the networks are not really of small-world type. Therefore we also consider a reduced network where we keep only nodes/states whose diagonal energies are relatively close to the diagonal energy of the hub, i.e. such that the energy condition $|(H_I)_{ii} - (H_I)_{\text{hub,hub}}| < 1.5\Delta_1$ for the hub = 5720 is satisfied and where Δ_1 is the effective rescaled average one-particle level spacing introduced in Section 2 (see text below Eq. (5)). We remind that Δ_1 is small compared to the overall energy band width but typically large compared to the many body level spacing and also with respect to the effective level spacing of directly interaction coupled states [22,53]. As a consequence of this condition the effective dimension or network size of remaining nodes/states is considerably reduced to values ~ 4000 for the SYK case or ~ 1000 for the three cases with $V = \sqrt{14}$. The modified distributions for this reduced network of link number N_l and Erdős

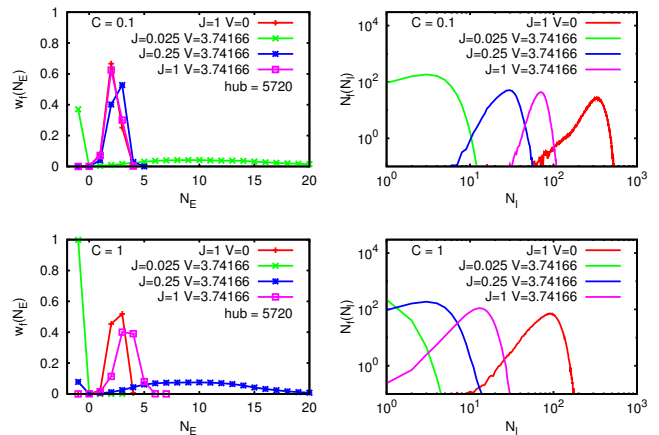


Fig. 10. (color online) Frequency distribution $N_f(N_l)$ of link number N_l per node (right panels) and probability distribution $w_f(N_E)$ of Erdős number N_E (left panels) for an effective network constructed from H_I as in Fig. 8 but only using nodes/states satisfying the energy condition: $|(H_I)_{ii} - (H_I)_{\text{hub,hub}}| < 1.5\Delta_1$ for hub = 5720. Color of curves/data points is red (SYK, $V = 0$, $J = 1$), green ($V = \sqrt{14}$, $J = 0.025$), blue ($V = \sqrt{14}$, $J = 0.25$) and pink ($V = \sqrt{14}$, $J = 1$). For these four cases respectively the mean and the width of the distribution of N_l are: 323 ± 67 , 3.50 ± 1.87 , 28.8 ± 7.0 , 69.9 ± 10.4 ($C = 0.1$, top right panel) and 89.3 ± 23.4 , 0.368 ± 0.603 , 3.50 ± 1.90 , 13.4 ± 4.0 ($C = 1$, bottom right panel); the mean and the width of the distribution of N_E (not counting $N_E = -1$ cases) are: 2.18 ± 0.56 , 12.0 ± 6.1 , 2.54 ± 0.63 , 2.23 ± 0.58 ($C = 0.1$, top left panel) and 2.51 ± 0.55 , 0.371 ± 0.622 , 10.2 ± 4.5 , 3.41 ± 0.85 ($C = 1$, bottom left panel); the average effective dimension/reduced network size is: 4107, 869, 883, 1102 (all panels). Left panels show the probability distribution $w_f(N_E)$ normalized to unity for a better visibility as compared to $N_f(N_E)$ (shown in Figs. 8 and 9) with different normalizations due to different network sizes. As in Fig. 8 the case $N_E = -1$ represents nodes which cannot be reached by the hub. All curves were obtained from an average over the same 100 different random realizations of H_I ($M = 16$, $L = 7$, $d = 11440$) used in Fig. 8.

number N_E are shown in Fig. 10. The frequency distribution $N_f(N_l)$ is similar as in Fig. 8 with a clear ordering of typical sizes from strongest coupling (SYK) to weakest coupling ($V = \sqrt{14}$ and $J = 0.025$) and an overall shift from $C = 0.1$ to $C = 1$. The distribution of Erdős numbers for SYK is not changed (apart from the modified normalization) while the cases with $V = \sqrt{14}$ are now generally closer to a small-world situation. Here $J = 1$ is now identical (close) to SYK, $J = 0.25$ provides typical Erdős numbers $\sim 2 - 3$ (~ 10), and the case $J = 0.025$ corresponds to a typical Erdős number ~ 12 (majority of nodes isolated from hub) all for $C = 0.1$ ($C = 1$). This clearly confirms that large Erdős numbers $\sim 10^2$ of the full network before correspond to diffusion to other energy layers.

The data of Figs. 8-10 clearly show that the TBRIM is characterized by small-world properties provided the in-

interaction strength is sufficiently large. Especially the SYK case with an average Erdős number $\langle N_E \rangle = 2.2 \pm 0.5$ (3.4 ± 1) for $C = 0.1$ ($C = 1$) shows very strong small-world properties. However, for modest interaction strength there are some complications due to diffusion in energy space leading to possible Erdős numbers $\sim 10^2$. We think that the further development of the analogy between quantum many-body interacting systems and small-world networks will bring a better understanding of these quantum systems.

We note that the small-world network constructed for an energy layer of a finite width (we use the width of $3\Delta_1$) is more relevant for the qubit relaxation analyzed in previous Sections: the coupling of the qubit with the states inside this layer leads to its rapid relaxation on the time scale related to $\Gamma_c \sim \Delta_1$, while slow transitions from one energy layer to another layer describe the residual level of density matrix relaxation analyzed in the next Section.

6 Residual level of density matrix relaxation

Our TBRIM model contains a finite number of states d and hence the relaxation of density matrix components stops at a certain residual level of density matrix elements $|\rho_{01}|$ determined by quantum deterministic fluctuations and noise. In fact since the spectrum of our system is discrete and the system is bounded we will always have the Poincaré recurrences to the initial state in agreement with the Poincaré recurrence theorem [63]. However, the time t_r of such a recurrence grows exponentially with the system size $\ln t_r \propto d$ being enormously large even for our case with $L = 7$ particles. However, depending on the initial state and parameters it is possible that the effective number d_{eff} of excited states contributing in the exact time evolution is much smaller than d implying that for these cases t_r is strongly reduced. Therefore we compute the deterministic residual level of quantum fluctuations given by $|\rho_{01}|$ averaged over long times for $d/4 \leq t/\Delta t \leq d/2$ roughly corresponding to $t_H/2 \leq t \leq t_H$ (or $|\rho_{00} - 1/2|$ with similar results).

The dependence of the residual level of quantum fluctuations on J, m is shown in Fig. 11. The lowest level is at the middle of energy band with $m = 5720$ corresponding to infinite temperature T . The highest level is found for the ground state $m = 0$ and first excited states $m = 1, 2$ with $J < 1$ at $V = \sqrt{14}$. The amplitude of residual fluctuations decreases with increase of J but it is difficult to establish a clear border in (J, m) plane. We attribute this to the fact that the Åberg border (1) works mainly for small J values with $g \gg 1$ so that a special analysis of this region is required that was not the main aim of this work.

We note that the residual fluctuations are rather similar for the SYK regime at $J > 10$ and the quantum dot regime above the Åberg border (1) with $0.15 \leq J < 10$ (except very low excited levels $m < 7$ and $J < 0.5$). We attribute this to the fact that in this region $\Gamma_c \gg \Delta_1$ leading to the explosive spreading over the quantum small-world.

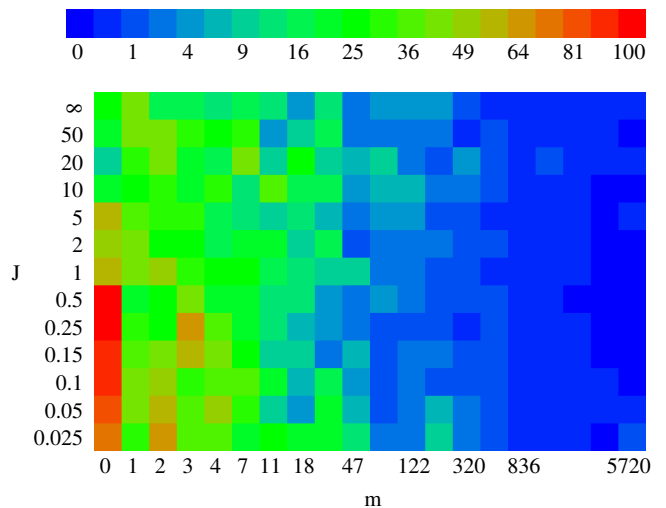


Fig. 11. (color online) Density plot of residual level of quantum fluctuations determined as the time average of $|\rho_{01}(t)|$ at long times for $d/4 \leq t/\Delta t \leq d/2$. The horizontal axis corresponds to the level number $m = 0, 1, 2, 3, 4, 7, 11, 18, 29, 47, 76, 122, 198, 320, 517, 836, 1353, 2187, 3537, 5720$ of the initial state (10) and the vertical axis corresponds to the value of the interaction strength J at $V = \sqrt{14} \approx 3.74166$ except for the top row (with symbol “ $J = \infty$ ”) representing the SYK case $J = 1$ and $V = 0$. The coupling strength is $\varepsilon = 0.03$. The colors red, green or blue correspond to maximum $|\rho_{01}(t)| = 0.4353$, intermediate or minimum (zero) fluctuation values (they are shown by color bar on top with numbers showing the percentage of maximal value).

In analogy with [8] we expect that in the regime of developed quantum chaos the residual level R_q of quantum fluctuations of qubit drops as a square-root of the states of a detector $R_q \propto 1/\sqrt{d}$. However, the quantum computations for TBRIM detector are more complicated compared to the kicked rotator case and we did not performed detailed numerical checks of this relation which is however in a qualitative agreement with the results of Fig. 11.

Finally we make a note on the relaxation dependence of the qubit energy given by 2δ . Above we presented results for a fixed value $\delta = \Delta_1$ but we checked that the relaxation of density matrix components goes in a similar manner for other values of the ratio $0.3 \leq 2\delta/\Delta_1 < 3$ as it is shown in Fig. 12. The changes of the decay curves start to be visible for $2\delta/\Delta_1 \geq 3$ but in this range the qubit energy becomes comparable to the energy size of the TBRIM band that corresponds to another physical regime where the qubit cannot be considered as a weak perturbation.

We also mention that our above discussion of the properties of qubit relaxation concern the range of positive temperatures with $m \leq d/2$. The regime of negative temperatures is briefly discussed in Appendix C where we find comparable results for the qubit relaxation as in the regime of positive temperatures. This is also in agreement with spin relaxation at negative temperatures considered in [64].

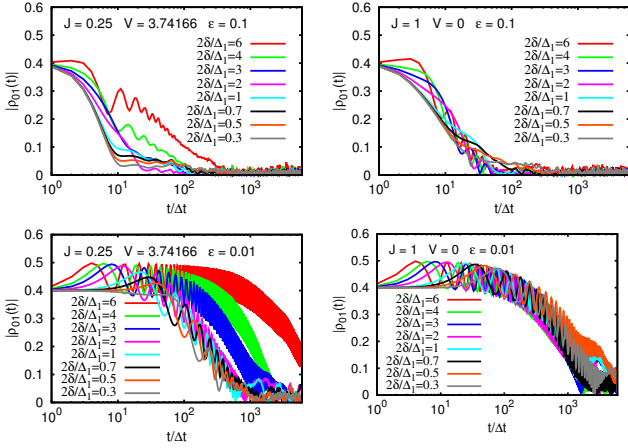


Fig. 12. (color online) Time dependence of $|\rho_{01}(t)|$ at level number $m = 5720$ for the initial state in (10) for various values of the parameter δ according to: $0.3 \leq 2\delta/\Delta_1 \leq 6$. The horizontal axis for the time is shown in logarithmic representation for a better visibility. Top (bottom) panels correspond to coupling strength $\varepsilon = 0.1$ (0.01). Left (right) panels correspond to $V = 3.74166$, $J = 1$ ($V = 0$, $J = 1$).

7 Discussion

We presented results for a dynamical decoherence of a qubit weakly coupled to the TBRIM system in the regime of dynamical thermalization induced by interactions and quantum many-body chaos, corresponding to the quantum dot of interacting fermions and the SYK black hole model. The relaxation rates of qubit population Γ_1 and dephasing Γ_2 are determined as a function of qubit coupling strength ε with $\Gamma_1 \propto \varepsilon^2$ in the Fermi golden rule regime and $\Gamma_1 \propto 1/\varepsilon$ in the quantum Zeno regime with $\Gamma_2 \propto \varepsilon^2$ for the whole considered range. These results are in a satisfactory agreement with the usual thermal bath qubit decoherence considered in the literature (see e.g. [6]). The surprising finding of our studies is that the values of Γ_1, Γ_2 remain practically unchanged in a broad range of parameters of the quantum dot or the SYK model. We propose a tentative explanation of this effect by tracing an analogy between TBRIM system and quantum small-world networks with appearance of explosive spreading over exponential number of sites (states) in a finite time. This explosive spreading appears in both regimes of quantum dot and SYK when the transition rates between directly coupled states become larger than an effective level spacing between one-particle states. We hope that our results will stimulate further investigations of dynamical decoherence in quantum many-body interacting systems and a further development of parallels between these systems and the small-world networks.

This work was supported in part by the Programme Investissements d’Avenir ANR-11-IDEX-0002-02, reference ANR-10-LABX-0037-NEXT (project THETRACOM); it was granted access to the HPC resources of CALMIP (Toulouse) under the allocation 2017-P0110.

APPENDIX

A Gaussian density of states

A.1 Analytical computation of the variance

The TBRIM Hamiltonian H_I given by (2) exhibits in the limit $M \rightarrow \infty$ at a fixed value of particle number L an average density of states which is obviously Gaussian in absence of interaction ($J = 0$) since in this case the many body energy levels are given by $E(\{n_j\}) = \sum_j n_j \varepsilon_j$ with $n_j \in \{0, 1\}$ which is a sum of random Gaussian variables with vanishing average and variance:

$$\begin{aligned} \sigma_\varepsilon^2 &= \langle E(\{n_j\})^2 \rangle = \sum_{j,j'=1}^M n_j n_{j'} \langle \varepsilon_j \varepsilon_{j'} \rangle \\ &= \frac{1}{M} \sum_{j=1}^M n_j^2 V^2 = \frac{L}{M} V^2. \end{aligned} \quad (19)$$

However, the expression (19) requires to take the ensemble average over the one-particle energies ε_j , i.e. the numerical verification of the variance requires an average over many realizations and from a pure mathematical point of view the Gaussian form of the distribution of $E(\{n_j\})$ requires indeed the limit $M \rightarrow \infty$ at fixed value L (and of $V^2/M \rightarrow \text{const.}$) providing a sum of *independent* Gaussian variables.

On the other hand, we find numerically that the density of states is very close to a Gaussian distribution already for one sample of H_I at the values of M and L we considered. To understand this let us first consider $J = 0$ and let ε_j be one sample of one-particle energies initially drawn from a Gaussian distribution (with zero mean and variance V^2/M) and then slightly modified by a small universal shift and rescaling factor to ensure *exactly* that $\sum_j \varepsilon_j = 0$ and $\sum_j \varepsilon_j^2 = V^2$. Now we consider this set of one-particle energies fixed and perform the average of $E(\{n_j\})$ not with respect to ε_j but with respect to all configurations $n_j \in \{0, 1\}$ such that $L = \sum_j n_j$. In this case we have obviously $\langle n_j \rangle = L/M$. Furthermore we find:

$$L^2 = \sum_{j,j'=1}^M \langle n_j n_{j'} \rangle = M \langle n_j \rangle + M(M-1) \langle n_j n_{j'} \rangle_{j \neq j'} \quad (20)$$

where we have separated the terms with $j = j'$ from those with $j \neq j'$. From (20) we immediately find:

$$\langle n_j n_{j'} \rangle_{j \neq j'} = \frac{L(L-1)}{M(M-1)} \quad (21)$$

and therefore we get, for $J = 0$, a different variance with respect to (19):

$$\begin{aligned} \sigma^2(0) &= \langle E(\{n_j\})^2 \rangle = \frac{L}{M} \sum_{j=1}^M \varepsilon_j^2 + \frac{L(L-1)}{M(M-1)} \sum_{j \neq j'}^M \varepsilon_j \varepsilon_{j'} \\ &= \frac{L}{M} \left(1 - \frac{L-1}{M-1} \right) \sum_{j=1}^M \varepsilon_j^2 = \frac{L(M-L)}{M(M-1)} V^2. \end{aligned} \quad (22)$$

To obtain (22) we have used that:

$$\sum_{j \neq j'}^M \epsilon_j \epsilon_{j'} = \left(\sum_{j=1}^M \epsilon_j \right)^2 - \sum_{j=1}^M \epsilon_j^2 = - \sum_{j=1}^M \epsilon_j^2 \quad (23)$$

since $\sum_j \epsilon_j = 0$ by choice.

Now we consider a non-vanishing interaction strength $J \neq 0$. In the limit for sufficiently small J we expect that the density of states is not affected by J . If we assume that the density of states remains Gaussian, also for larger values of J , (see below for the numerical confirmation of this) we can compute the variance σ^2 from the average:

$$\begin{aligned} \sigma^2 &= \frac{1}{d} \int_{-\infty}^{\infty} E^2 \langle \rho(E) \rangle dE = \frac{1}{d} \left\langle \sum_{m=0}^{d-1} E_m^2 \right\rangle \\ &= \frac{1}{d} \langle \text{Tr}(H_I^2) \rangle = \sigma^2(0) + \frac{1}{d} \langle \text{Tr}(H_J^2) \rangle \end{aligned} \quad (24)$$

where E_m are the exact many body energies, $\sigma^2(0)$ is the variance at $J = 0$ given in (22) and

$$H_J = \frac{4}{\sqrt{2M^3}} \sum_{i < j, k < l} J_{ij,kl} c_i^\dagger c_j^\dagger c_l c_k \quad (25)$$

is the interaction contribution in (2). In (24) the average is done at fixed one-particle energies with respect to the different configurations of the occupation numbers n_j (satisfying $\sum_j n_j = L$) and with respect to the Gaussian interaction matrix elements $J_{ij,kl}$. To evaluate $(1/d) \langle \text{Tr}(H_J^2) \rangle$ let us consider one particular many body state where exactly L of the M orbitals are occupied. This state is coupled by the interaction to three groups of other states: (i) ‘‘itself’’, i.e. with identical occupation numbers n_j , (ii) $L(M-L)$ states that differ exactly for one particle occupying another orbital, and (iii) $L(L-1)(M-L)(M-L-1)/4$ states that differ exactly for two particles occupying other orbitals. This corresponds to a total number of coupled states $1 + L(M-L) + L(L-1)(M-L)(M-L-1)/4$, an expression already given in [22, 29].

However, in order to evaluate the contributions of the corresponding interaction matrix elements in $\langle \text{Tr}(H_J^2) \rangle$ this (global) number is not relevant since the average variance of the interaction matrix element differs between these three groups. The interaction matrix element of the state with itself, corresponding to the group (i), uses $L(L-1)/2$ terms of (25) since there are $L(L-1)/2$ possibilities to destroy a pair of particles in the set of given L particles and to recreate them afterwards in their same original orbitals. This corresponds to a sum of $L(L-1)/2$ independent Gaussian variables $J_{ij,ij}$ with variance¹ $2J^2$, giving a contribution in $\langle \text{Tr}(H_J^2) \rangle$ being $(8/M^3) J^2 L(L-1)$.

¹ It is mathematically also possible to consider other symmetry classes GUE or GSE for the interaction matrix which would imply a variance of $2J^2/\beta$ (with $\beta = 1$ for GOE, 2 for GUE and 4 for GSE) for the variables $J_{ij,ij}$ if we keep the non-diagonal variance J^2 of $J_{ij,kl}$ for $(ij) \neq (kl)$.

Concerning the group (ii), we need to consider in (25) the index pairs $i < j$ and $k < l$ where one index of the first pair is identical to one index of the other pair and the other one is different. This gives $L-1$ possibilities to destroy the pair of particles and recreate them afterwards such that one of the two particles stays in the same orbital and the other one has changed its orbital. Therefore the total contribution of all states of the group (ii) to $\langle \text{Tr}(H_J^2) \rangle$ is $(8/M^3) J^2 L(M-L)(L-1)$.

Concerning the group (iii) both indices must be different and there is only one term in (25) contributing to the interaction matrix element. Hence the total contribution of all states of the group (iii) to $\langle \text{Tr}(H_J^2) \rangle$ is $(8/M^3) J^2 L(L-1)(M-L)(M-L-1)/4$.

This argumentation does not depend on the choice of initial state giving a factor d canceling the factor $1/d$ in (24). Putting this all together, we obtain from (24) the expressions (3), (4) and (5) given in the main text for σ in terms of the effective energy scale V_{eff} and the coefficient $a(M, L)$ which measures the global energy rescaling due to finite values of J/V .

A.2 Numerical verification

In order to verify numerically the Gaussian density of states with the theoretical variance given in (3) it is more convenient to determine the integrated density of states:

$$P(E) = \frac{1}{d} \int_{-\infty}^E \rho(\tilde{E}) d\tilde{E}. \quad (26)$$

The prefactor $1/d$ assures the limit $\lim_{E \rightarrow \infty} P(E) = 1$ since $\rho(E)$ is chosen to be normalized to d and not unity. In case of an ideal Gaussian density of states, as in (3), we have:

$$P(E) = P_{\text{gauss}}(E) = \frac{1}{2} \left(1 + \text{erf} \left(\frac{E}{\sqrt{2}\sigma} \right) \right) \quad (27)$$

with $\text{erf}(x) = (2/\sqrt{\pi}) \int_0^x \exp(-y^2) dy$.

If E_m represent the numerically computed eigenvalues (of one sample of H_I and ordered in increasing order with level number $m = 0, \dots, d-1$) the integrated density of states is simply obtained by drawing the quantity $z_m = (m+0.5)/d$ versus E_m which gives the appearance of a rather smooth curve for a sufficiently large value of d which can be compared to the expression (27). In order to perform a more sophisticated fit analysis we generalize (27) to:

$$P_k(E) = \frac{1}{2} \left(1 + \text{erf} \left(q_k(E)/\sqrt{2} \right) \right) \quad (28)$$

where $q_k(E)$ is a polynomial of degree k . The case $k = 1$ with $q_1(E) = (E - E_c)/\sigma_{\text{fit}}$ corresponds to a Gaussian density of states with variance σ_{fit} and center E_c . Choosing larger values of $k > 1$ we may analyze deviations with respect to the ideal Gaussian distribution. From the practical point of view a direct fit of z_m with $P_k(E_m)$

is a bit tricky because it is non-linear and it is easier to perform the least-square minimization not in the vertical but in the horizontal axis. To do this explicitly let, for $0 < x < 1$, the function $\text{inverf}(x)$ be defined as the inverse of $\text{erf}(x)$ such that $\text{erf}(\text{inverf}(x)) = x$. Then we apply the fit $q_k(E_m) = \sqrt{2} \text{inverf}(2z_m - 1)$ which is linear in the coefficients of the polynomial $q_k(E)$ and provides a unique well defined solution.

We have applied this fit for the two cases $k = 1$ and $k = 5$, for many different values the ratio J/V covering many orders of magnitude and our standard choice $M = 16$, $L = 7$ with $d = 11440$. In all cases the hypothesis of an approximate Gaussian density of states is well confirmed with a value of σ_{fit} confirming the theoretical expression in (3) with an error below 1%. As an additional verification, we have also numerically determined the variance from the trace, i.e. the quantity $\sigma_{\text{Tr}}^2 = (1/d)\text{Tr}(H_I^2) = (1/d)\sum_m E_m^2$ (the last equality is valid with numerical precision $\sim 10^{-14}$). In all cases σ_{Tr} also coincides with σ_{fit} and the theoretical expression with an error below 1%.

However, a careful comparison of the numerical curve of $P(E)$ with $P_1(E)$ shows small but systematic deviations which can be significantly reduced by increasing the degree of the fit polynomial $q_k(E)$. For $k = 5$ it is already nearly impossible to distinguish the numerical curve from $P_5(E)$ on graphical precision. This is clearly illustrated in Fig. 13 where we compare the numerical curve $P(E)$ with $P_1(E)$ and $P_5(E)$ for the two cases $J = 3.74166$, $V = 0.25$ and $V = 0$, $J = 1$ (SYK-case). In order to see the differences between the two fits it is actually necessary to draw the difference of $P(E) - P_k(E)$ in an increased scale as it is done in the lower panels of Fig. 13.

We attribute the small deviations to the Gaussian density of states to the finite values of M and L and also to the fact that we used only one numerical sample of H_J . Actually, for finite values of J it is to our knowledge still an open problem if the average density of states of H_I is indeed Gaussian even for the limit $M \rightarrow \infty$ and L finite (previous analytical results [44, 45] apply to the SYK-case with Majorana fermions that is different from our model at $V = 0$ and $J = 1$).

B Weakly excited initial states

The fit procedure using the fit functions (14), (15) to approximate $\rho_{11}(t)$ and $|\rho_{01}(t)|$ are very often quite problematic. First the non-linear fits with a considerable number of parameters depend rather strongly on “good” initial values, especially for the frequencies $\omega_{1,2}$, for the Levenberg-Marquardt iteration. Furthermore it is typically necessary to attribute stronger weights on the initial times. For this we typically perform a first simple exponential fit of the survival probability $p(t) = |\langle \psi(0) | \psi(t) \rangle|^2$ which provides a smooth simplified decay time which we use to fix exponentially decaying weights in time for the more precise fits using the fit functions (14), (15). For larger values of the couplings strength, typically at $\varepsilon \geq 0.1$, the periodic

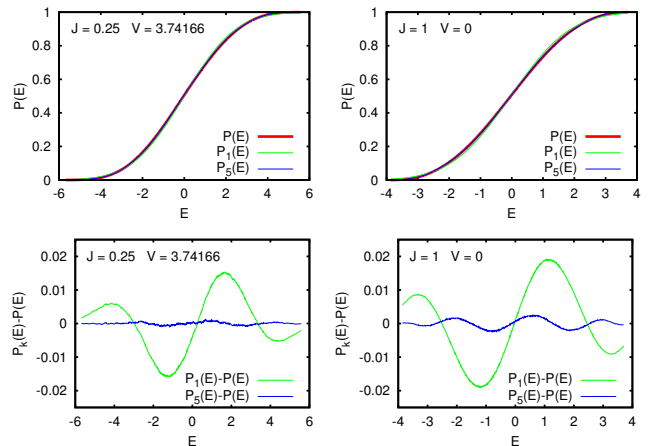


Fig. 13. (color online) Integrated density of states $P(E)$ of the TBRIM Hamiltonian (2) represented by the curve $z_m = (m + 0.5)/d$ versus energy level E_m (red curve) with $m = 0, \dots, d-1$ being the level number. The Hilbert space dimension is $d = 11440$ for $L = 7$ particles and $M = 16$ orbitals. Shown are the curves for one individual spectrum at $V = 3.74166$, $J = 0.25$ (top left panel) and the SYK-case $V = 0$, $J = 1$ (top right panel). The functions $P_k(E)$ correspond to the fit (28). Shown are the cases $k = 1$ (green curve) and $k = 5$ (blue curve). The case $k = 1$ corresponds to the (integrated) Gaussian density of states with two fit parameters for the width σ_{fit} and center E_c . The fits for $k = 1$ provide for $V = 3.74166$, $J = 0.25$ ($V = 0$, $J = 1$) the values $E_c = -0.008 \pm 0.001$ (-0.032 ± 0.001) and $\sigma_{\text{fit}} = 1.951 \pm 0.001$ (1.508 ± 0.001) giving the ratio $\sigma_{\text{fit}}/\sigma = 0.9983 \pm 0.0006$ (0.9952 ± 0.0008) where $\sigma = 1.954$ (1.516) is the theoretical value obtained from (3). For comparison the quantity σ_{Tr} , obtained numerically from the trace of H_I^2 , gives for both cases $\sigma_{\text{Tr}} = 1.947$ (1.503). In top panels the blue curves for $P_5(E)$ coincide with the red curves for $P(E)$ on graphical precision while the green curves for $P_1(E)$ are slightly above (below) the red curve for $E > 0$ ($E < 0$). Bottom panels show the difference $P_k(E) - P(E)$ of the fit functions with respect to the numerical function $P(E)$ for $k = 1$ (green curve) and $k = 5$ (blue curve) using an increased scale.

structure with the frequencies $\omega_{1,2}$ also disappears and the fits have to be simplified accordingly as mentioned in the main text.

Even, taking all this into account, for weakly excited initial states, with small values of the level number m in (10), the quality of the fits may be rather poor due to the absence of exponential decay, presence of a quasi-periodic structure or the effect that after an initial decrease $|\rho_{01}(t)|$ re-increases at sufficiently long times.

In Fig. 14 we show some examples of this type for the level number $m = 7$ at our usual standard parameters $V = 3.74166$, $J = 0.25$ or $V = 0$, $J = 1$ and the coupling strengths $\varepsilon = 0.01$ or 0.02 . The quantity $\rho_{11}(t)$ exhibits a structure with beats introducing a second smaller frequency which is only captured by $f_{11}(t)$ at the initial times and even here the deviations due to the non-exponential decay are quite well visible. For $|\rho_{01}(t)|$ there are fluctuations with long correlation times for larger time scales which are

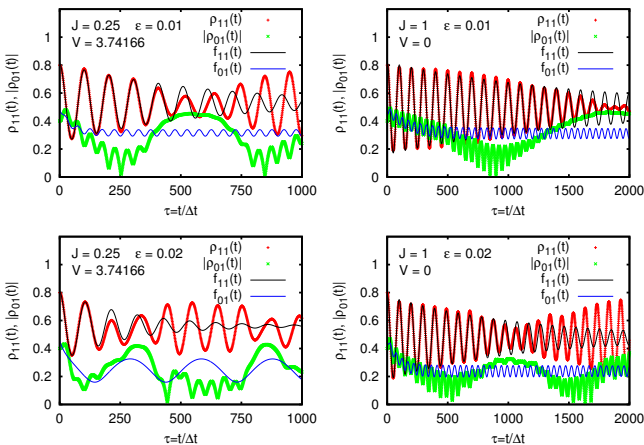


Fig. 14. (color online) Time dependence of $\rho_{11}(t)$ (red plus symbols), $|\rho_{01}(t)|$ (green crosses) and the two fit functions $f_{11}(t)$ (thin black line) and $f_{01}(t)$ (thin blue line), defined in (14) and (15), for level number $m = 7$ of the initial state (10) and $V = 3.74166$, $J = 0.25$ ($V = 0$, $J = 1$) in left (right) panels at coupling strength $\varepsilon = 0.01$ (0.02) in top (bottom) panels. As in Figs. 2, 3 the time is measured in units of Δt and the number of particles (orbitals) is $L = 7$ ($M = 16$).

not well captured by the periodic saturated form of $f_{01}(t)$ at long times. In one case at $J = 0.25$, $V = 3.74166$ and $\varepsilon = 0.02$, the frequency ω_2 is considerably reduced to fit the long range form of $|\rho_{01}(t)|$ but this effect does not reflect the physical reality and provides poor values of the two decay rates Γ_2 and $\tilde{\Gamma}_2$.

Due to these effects, we do not show any fit functions in Fig. 2, which applies to the level number $m = 0$, and in Figs. 4 and 5 we show the decay rate for the largest level number $m = 5720$ which is not problematic as can be seen in Fig. 3. Furthermore in Figs. 6 and 7, we only show data points for $m > 100$.

C Initial state with negative temperature

In Fig. 15 we present the results for qubit relaxation in the regime of negative temperature (initial state is above the half of energy band width). Here the dynamical temperature of the initial state is $T = 1/\beta$; $\beta = -0.5424$. We see that the relaxation is practically the same as for the initial state with positive temperature at $\beta = 0.5443 = 1/T$. This effect is due to symmetry between negative (positive derivative of the density of states) and positive energies (negative derivative of the density of states). The former correspond to positive and the latter to negative temperatures as can also be seen in the bottom panels of Fig. 1.

References

1. V.B. Braginsky and F.Ya. Khalili, *Quantum measurement*, Cambridge University Press, Cambridge, UK (1992).

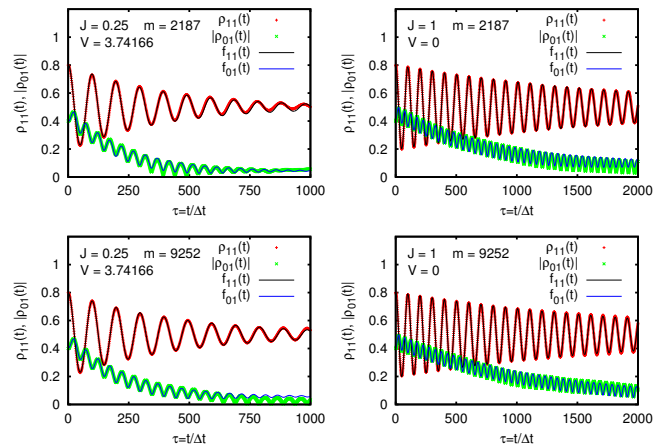


Fig. 15. (color online) Time dependence of $\rho_{11}(t)$ (red plus symbols), $|\rho_{01}(t)|$ (green crosses) and the two fit functions $f_{11}(t)$ (thin black line) and $f_{01}(t)$ (thin blue line), defined in (14) and (15), for coupling strength $\varepsilon = 0.01$ and $V = 3.74166$, $J = 0.25$ ($V = 0$, $J = 1$) in left (right) panels at level numbers $m = 2187$ (9252) in top (bottom) panels. The initial state for $V = 3.74166$, $J = 0.25$ at level number $m = 2187$ (9252) corresponds to the inverse temperature $\beta = 0.5443$ (-0.5424). As in Figs. 2, 3 the time is measured in units of Δt and the number of particles (orbitals) is $L = 7$ ($M = 16$).

2. M.A. Nielsen and I.J. Chuang, *Quantum computation and quantum information*, Cambridge University Press, Cambridge, UK (2000).
3. Y. Nakamura, Yu. Pashkin and J.S. Tsai, *Coherent control of macroscopic quantum states in a single-Cooperpair box*, Nature **398**, 786 (1999).
4. D. Vion, A. Aassime, A. Cottet, P. Joyez, H. Pothier, C. Urbina, D. Esteve and M.H. Devoret, *Manipulating the quantum state of an electrical circuit*, Science **296**, 886 (2002).
5. A.N. Korotkov and D.V. Averin, *Continuous weak measurement of quantum coherent oscillations*, Phys. Rev. B **64**, 165310 (2001).
6. Yu. Makhlin, G. Schön and A. Shnirman, *Quantum state engineering with Josephson-junction devices*, Rev. Mod. Phys. **73**, 357 (2001).
7. G. Wendin, *Quantum information processing with superconducting circuits: a review*, Rep. Prog. Phys. **80**, 106001 (2017).
8. J. W. Lee, D. V. Averin, G. Benenti and D. L. Shepelyansky, *Model of a deterministic detector and dynamical decoherence*, Phys. Rev. A **72**, 012310 (2005).
9. E. Wigner, *Random matrices in physics*, SIAM Rev. **9**(1), 1 (1967).
10. M.L. Mehta, *Random matrices*, Elsevier Academic Press, Amsterdam (2004).
11. T. Guhr, A. Müller-Groeling and H.A. Weidenmüller, *Random-matrix theories in quantum physics: common concepts*, Phys. Rep. **299**, 189 (1998).
12. O. Bohigas, M.J. Giannoni and C. Schmit, *Characterization of chaotic quantum spectra and universality of level fluctuation*, Phys. Rev. Lett. **52**, 1 (1984).
13. F. Haake, *Quantum signatures of chaos*, Springer, Berlin (2010).

14. D. Ullmo, *Bohigas-Giannoni-Schmit conjecture*, Scholarpedia **11**(9), 31721 (2016).
15. J.B. French, and S.S.M. Wong, *Validity of random matrix theories for many-particle systems*, Phys. Lett. B **33**, 449 (1970).
16. O. Bohigas and J. Flores, *Two-body random Hamiltonian and level density*, Phys. Lett. B **34**, 261 (1971).
17. J.B. French, and S.S.M. Wong, *Some random-matrix level and spacing distributions for fixed-particle-rank interactions*, Phys. Lett. B **35**, 5 (1971).
18. O. Bohigas and J. Flores, *Spacing and individual eigenvalue distributions of two-body random Hamiltonians*, Phys. Lett. B **35**, 383 (1971).
19. S. Åberg, *Onset of chaos in rapidly rotating nuclei*, Phys. Rev. Lett. **64**, 3119 (1990).
20. S. Åberg, *Quantum chaos and rotational damping*, Prog. Part. Nucl. Phys. **28**, 11 (1992).
21. D.L. Shepelyansky and O.P. Sushkov, *Few interacting particles in a random potential*, Europhys. Lett. **37**, 121 (1997).
22. P. Jacquod and D.L. Shepelyansky, *Emergence of quantum chaos in finite interacting Fermi systems*, Phys. Rev. Lett. **79**, 1837 (1997).
23. B. Georgeot and D.L. Shepelyansky, *Integrability and quantum chaos in spin glass shards*, Phys. Rev. Lett. **81**, 5129 (1998).
24. B. Georgeot and D.L. Shepelyansky, *Quantum chaos border for quantum computing*, Phys. Rev. E **62**, 3504 (2000).
25. D.L. Shepelyansky, *Quantum chaos and quantum computers*, Physica Scripta **T90**, 112 (2001).
26. G. Benenti, G. Casati and D.L. Shepelyansky, *Emergence of Fermi-Dirac thermalization in the quantum computer core*, Eur. Phys. J. D **17**, 265 (2001).
27. I.V. Gornyi, A.D. Mirlin and D.G. Polyakov, *Many-body delocalization transition and relaxation in a quantum dot*, Phys. Rev. B **93**, 125419 (2016).
28. I.V. Gornyi, A.D. Mirlin, D.G. Polyakov and A.L. Burin, *Spectral diffusion and scaling of many-body delocalization transitions*, Ann. Phys. (Berlin) **529**, 1600360 (2017)
29. V.B. Flambaum and F.M. Izrailev, *Distribution of occupation numbers in finite Fermi systems and role of interaction in chaos and thermalization*, Phys. Rev. E **55**, R13(R) (1997).
30. L.D. Landau and E.M. Lifshitz, *Statistical mechanics*, Wiley, New York (1976).
31. M. Mulansky, K. Ahnert, A. Pikovsky and D.L. Shepelyansky, *Dynamical thermalization of disordered nonlinear lattices*, Phys. Rev. E **80**, 056212 (2009).
32. L. Ermann and D.L. Shepelyansky, *Quantum Gibbs distribution from dynamical thermalization in classical nonlinear lattices*, New J. Phys. **15**, 123004 (2013).
33. P. Schlageck and D.L. Shepelyansky, *Dynamical thermalization in Bose-Hubbard systems*, Phys. Rev. E **93**, 012126 (2016).
34. A.R. Kolovsky and D.L. Shepelyansky, *Dynamical thermalization in isolated quantum dots and black holes*, EPL **117**, 10003 (2017).
35. R. Nandkishore and D.A. Huse, *Many-body localization and thermalization in quantum statistical mechanics*, Annu. Rev. Condens. Matter Phys. **6**, 15 (2015).
36. L. D. Alessio, Y. Kafri, A. Polkovnikov and M. Rigol, *From quantum chaos and eigenstate thermalization to statistical mechanics and thermodynamics*, Adv. Phys. **65**, 239 (2016).
37. F. Borgonovi, F.M. Izrailev, L.F. Santos and V.G. Zelevinsky, *Quantum chaos and thermalization in isolated systems of interacting particles*, Phys. Rep. **626**, 1 (2016).
38. F. Alet and N. Laflorencie, *Many-body localization: an introduction and selected topics*, arXiv:1711.03145 [cond-mat.str-el] (2017).
39. S. Sachdev and J. Ye, *Gapless spin-fluid ground state in a random quantum Heisenberg magnet*, Phys. Rev. Lett. **70**, 3339 (1993).
40. A. Kitaev, *A simple model of quantum holography*, Video talks at KITP Santa Barbara, April 7 and May 27 (2015).
41. S. Sachdev, *Bekenstein-Hawking entropy and strange metals*, Phys. Rev. X **5**, 041025 (2015).
42. J. Polchinski and V. Rosenhaus, *The spectrum in the Sachdev-Ye-Kitaev model*, JHEP **04**, 1 (2016).
43. J. Maldacena and D. Stanford, *Remarks on the Sachdev-Ye-Kitaev model*, Phys. Rev. D **94**, 106002 (2016).
44. J.S. Cotler, G. Gur-Ari, M. Hanada, J. Polchinski, P. Saad, S.H. Shenker, D. Stanford, A. Streicher and M. Tezuka, *Black holes and random matrices*, JHEP **05**, 118 (2017).
45. A.M. Garcia-Garcia and J.J.M. Verbaarschot, *Spectral and thermodynamic properties of the Sachdev-Ye-Kitaev model*, Phys. Rev. D **94**, 126010 (2016).
46. A.M. Garcia-Garcia and J.J.M. Verbaarschot, *Analytical spectral density of the Sachdev-Ye-Kitaev model at finite N*, Phys. Rev. D **96**, 066012 (2017).
47. T. Kanazawa and T. Wettig, *Complete random matrix classification of SYK models with N= 0, 1 and 2 supersymmetry*, JHEP **09**, 50 (2017).
48. D. Harlow, *Jerusalem lectures on black holes and quantum information*, Rev. Mod. Phys. **88**, 015502 (2016).
49. B. Misra and E.C.G. Sudarshan, *The Zeno's paradox in quantum theory*, J. Math. Phys. **18**, 756 (1977).
50. M.C. Fischer, B. Gutiérrez-Medina and M.G. Raizen, *Observation of the quantum Zeno and anti-Zeno effects in an unstable system*, Phys. Rev. Lett. **87**, 040402 (2001).
51. A. Gusev, R.A. Jalabert, H.M. Pastawski and D.A. Wisniacki, *Loschmidt echo*, Scholarpedia **7**(8), 11687 (2012).
52. P. Jacquod, P.G. Silvestrov and C.W.J. Beenakker, *Golden rule decay versus Lyapunov decay of the quantum Loschmidt echo*, Phys. Rev. E **64**, 055203(R) (2001).
53. B. Georgeot and D. L. Shepelyansky, *Breit-Wigner width and inverse participation ratio in finite interacting Fermi systems*, Phys. Rev. Lett. **79**, (1997), 4365.
54. S. Milgram, *The small-world problem*, Psychology Today **1**(1), 61 (May 1967).
55. S. Dorogovtsev, *Lectures on complex networks*, Oxford University Press, Oxford (2010).
56. O. Giraud, B. Georgeot and D.L. Shepelyansky, *Quantum computing of delocalization in small-world networks*, Phys. Rev. E **72**, 036203 (2005).
57. L. Backstrom, P. Boldi, M. Rosa, J. Ugander and S. Vigna, *Four degrees of separation*, Proc. 4th ACM Web Sci. Conf., ACM N.Y. p.33 (2012).
58. L. Ermann, K.M. Frahm and D.L. Shepelyansky, *Google matrix analysis of directed networks*, Rev. Mod. Phys. **87**, 1261 (2015).
59. B. Georgeot and D.L. Shepelyansky, *Emergence of quantum chaos in the quantum computer core and how to manage it*, Phys. Rev. E **62**, 6366 (2000).
60. I. Garcia-Mata, O. Giraud, B. Georget, J. Martin, R. Dubertrand and G. Lemarie, *Scaling theory of the Anderson transition in random graphs: ergodicity and universality*, Phys. Rev. Lett. **118**, 166801 (2017).

61. P. Prelovsek, O.S. Barisic and M. Mierzejewski, *Reduced-basis approach to many-body localization*, Phys. Rev. B **97**, 035104 (2018).
62. P. Erdős and A. Rényi, *On random graphs I*, Publicationes Mathematicae **6**, 290 (1959).
63. H. Poincaré, *Sur le probleme des trois corps et les équations de la dynamique*, Acta Math. **13**, 1 (1890).
64. A. Abragam, *The principles of nuclear magnetism*, Oxford University Press, Oxford UK (1961).